PHYSICAL REVIEW D **89,** 015015 (2014)

Confronting the natural NMSSM with LHC7-8 data

Taoli Cheng,[1] Jinmian Li,[1,*] Tianjun Li,[1,2,3] and Qi-Shu Yan[4,5]

[1]*State Key Laboratory of Theoretical Physics, Institute of Theoretical Physics, Chinese Academy of Sciences, Beijing 100190, People's Republic of China*

[2]*School of Physical Electronics, University of Electronic Science and Technology of China, Chengdu 610054, People's Republic of China*

[3]*George P. and Cynthia W. Mitchell Institute for Fundamental Physics and Astronomy, Texas A&M University, College Station, Texas 77843, USA*

[4]*School of Physics Sciences, University of Chinese Academy of Sciences, Beijing 100049, China*

[5]*Center for High Energy Physics, Peking University, Beijing 100871, China*

(Received 22 April 2013; published 22 January 2014)

The natural supersymmetry (SUSY) requires that the stop, sbottom, and gluino are around 1 TeV or lighter. By using the direct SUSY search bounds from both the ATLAS and CMS collaborations, we examine the constraints on the natural SUSY in the next to minimal supersymmetric Standard Model. We consider two cases of interpretations for the Higgs boson data: (1) the Standard Model (SM)-like Higgs boson is the lightest *CP*-even Higgs boson; (2) the SM-like Higgs boson is the second lightest *CP*-even Higgs boson. We choose 2400 points or so to perform a detailed Monte Carlo simulation analysis, and we observe that the direct SUSY searches at the LHC impose a strong constraint on these light gluino scenarios.

DOI: 10.1103/PhysRevD.89.015015 PACS numbers: 12.60.Jv, 14.80.Da, 14.80.Ly

I. INTRODUCTION

As a leading candidate for new physics at the TeV scale, supersymmetry (SUSY) is strongly motivated by solving the quadratic divergence of the Standard Model (SM) as well as by providing a dark matter candidate and a radiative electroweak symmetry breaking mechanism. Compared with the situation before the startup of the LHC, the discovery of a Higgs boson [1,2] and the significant constraints from the direct SUSY search at the LHC have driven a drastic paradigm shift in the landscape of low energy supersymmetry [3,4]. We now know that the first two generation squarks must be heavier than 1.5 TeV, though it is too early to claim the death of low energy SUSY. It should be noted that the models with light third generation squarks and/or light gluinos, such as the natural SUSY models [5], nonuniversal gaugino models [6], and compressed SUSY models [7], can still be consistent with experimental data.

The Higgs boson discovered by both the ATLAS [1] and CMS [2] Collaborations can impose significant constraints on some SUSY models. For example, the naive gauge-mediated supersymmetry breaking and anomaly-mediated supersymmetry breaking models may not produce a SM-like Higgs boson with mass around 125 GeV [8] unless stops are very heavy because of the small trilinear soft A_t term. (For solutions, see Refs. [9,10].) Meanwhile, the constrained minimal supersymmetric Standard Model (MSSM) or the minimal supergravity (mSUGRA) model may be plagued by the fine-tuning issue in order to accommodate the Higgs boson mass [11] via loop-induced contributions. The so-called fine-tuning issue can be greatly alleviated in the next-to MSSM (NMSSM) [12] by utilizing both the tree-level free parameters and loop contributions [13–17]. Several ways to reduce the fine-tuning in the generalized NMSSM have been explored in [18].

In addition to alleviating the fine-tuning issue in the MSSM, the NMSSM is well motivated by solving the μ problem in the MSSM (for a review see [19]). The singlino can ease the tension between experimental data in dark matter searches and SUSY models (see [20] for a more detailed discussion). The NMSSM can be embedded into more fundamental theories, say the F-theory inspired grand unified theories (GUTs). The F-theory GUTs can induce unified boundary conditions on free parameters of the NMSSM and can yield interesting low energy phenomenologies, as explored in [21].

The renormalizable superpotential in the NMSSM with Z_3 symmetry is

$$W_{\rm NMSSM} = h_u \hat{H}_u \hat{Q} \hat{U}^c_R + h_d \hat{H}_d \hat{Q} \hat{D}^c_R + h_e \hat{H}_d \hat{L} \hat{E}^c_R + \lambda \hat{S} \hat{H}_u \hat{H}_d + \frac{\kappa}{3} \hat{S}^3, \quad (1)$$

where $\hat{Q}$, $\hat{U}^c_R$, $\hat{D}^c_R$, $\hat{L}$, $\hat{E}^c_R$, $\hat{H}_u$, $\hat{H}_d$ are the superfields for the quark doublet, the right-handed up-type quark, the right-handed down-type quark, the lepton doublet, the right-handed charged lepton, the up-type Higgs doublet, and the down-type Higgs doublet, respectively. The last term is needed to avoid the presence of a Goldstone boson by breaking the following global $U(1)$ Peccei-Quinn symmetry,

$$H_u H_d \to e^{i\alpha} H_u H_d, \quad S \to e^{-i\alpha} S. \quad (2)$$

*jmli@itp.ac.cn

The bilinear Higgs field mass μ term is forbidden by Z_3 symmetry. After the singlet Higgs field gets a vacuum expectation value (VEV) around the electroweak (EW) scale, the effective μ term can be generated naturally at the order of $\sim O(100)$ GeV. Although the Z_3 symmetry breaking usually leads to a cosmological domain wall problem, this problem can be solved by either adding a nonrenormalizable term in the superpotential [22] or by introducing an extra $U(1)$ gauge symmetry [23–26].

The exact supersymmetry must be broken at some high energy scales in the hidden sector and then it is mediated to the observable sector. The low energy supersymmetry breaking gaugino masses, scalar masses, and trilinear soft terms are

$$\begin{aligned}-\mathcal{L}_{\text{soft}}(\text{NMSSM}) = &\frac{1}{2}(M_3\tilde{g}\,\tilde{g} + M_2\tilde{W}\,\tilde{W} + M_1\tilde{B}\,\tilde{B} + \text{H.c.}) + m_{H_u}^2 H_u^* H_u + m_{H_d}^2 H_d^* H_d + m_S^2 S^* S \\ &+ \tilde{Q}^\dagger m_Q^2 \tilde{Q} + \tilde{U}_R^\dagger m_U^2 \tilde{U}_R + \tilde{D}_R^\dagger m_D^2 \tilde{D}_R + \tilde{L}^\dagger m_L^2 \tilde{L} + \tilde{E}_R^\dagger m_E^2 \tilde{E}_R \\ &+ \left(h_u A_u Q H_u U_R^c - h_d A_d Q H_d D_R^c - h_e A_e L H_d E_R^c + \lambda A_\lambda H_u H_d S + \frac{1}{3}\kappa A_\kappa S^3 + \text{H.c.}\right), \end{aligned} \tag{3}$$

where $\tilde{g}$, $\tilde{W}$, and $\tilde{B}$ are the gluino, Wino, and Bino, respectively. Roughly speaking, to avoid the so-called fine-tuning issue, the masses of superpartners are assumed to be a few hundreds of GeV and up to a few TeV.

The existence of an extra SM singlet in the NMSSM can lead to a richer Higgs phenomenology when compared with that of the MSSM. There are three *CP*-even Higgs bosons and two *CP*-odd Higgs bosons. We notice that both light *CP*-even neutral Higgs bosons (labeled as H_1 and H_2, respectively) can be SM-like. As pointed out in [27], the NMSSM can accommodate Higgs boson data quite well if the Higgs boson data observed by the ATLAS and CMS Collaborations were contributed by two degenerate Higgs bosons which have masses around 126 GeV. Moreover, the NMSSM has a better chance of interpreting an extra 98 GeV Higgs boson or an extra 136 GeV Higgs boson suggested by the LEP data [28] or the Tevatron data [29]. It is well known that the parameter space of either H_1 or H_2 being SM-like is different,[1] which motivates us to investigate these two cases separately.

The null results of the SUSY search at the LHC significantly and meaningfully constrain the masses of colored supersymmetric particles [32,33]. The experimental groups usually present their results in the constrained minimal supersymmetric standard model (CMSSM) and some simplified models without considering any other physical constraints. Recently, quite a few efforts have been devoted to interpreting the LHC search bounds on both the MSSM [34–37] and the NMSSM [20,38] with full low energy physical constraints. In these works, the first two generation squarks are usually excluded up to about 1.4–1.5 TeV. Nevertheless, the bounds on the third generation squarks are weaker because of their small production rates [20,39]. The gluino, which is already excluded up to 1.4 TeV in some constrained models, can be as light as ~500 GeV, if the mass spectrum is compressed [40,41]. All these features are consistent with the natural SUSY spectrum, which motivates us to examine various scenarios of the natural SUSY, where the third generation squarks and gluino may be light.

The light gluino can play important roles in radiative electroweak symmetry breaking, dark matter relic density, and gauge coupling unification at high scales. Light gluino scenarios can be well motivated by GUTs and string models, for example, the intersecting D-brane models [42–44], the F-theory GUTs [45,46], the G2-MSSM [47], the unnatural SUSY [48,49], the split SUSY scenario [50–54] [as well as the PeV (split) SUSY scenario [55]], the natural SUSY proposed in [5], the hidden SUSY scenario [56], and the compressed SUSY scenario [7].

Because of the large production rate of gluino pairs, the light gluino scenarios have been a focus of phenomenological research. Its discovery potential at the early LHC runs has been explored in the literature. For example, in Ref. [57], the signature of a long-lived gluino under the split SUSY has been explored. As shown in Ref. [58], a broad and diverse sample of light gluino scenarios (from 350 GeV to 700 GeV) in minimal and nonminimal supergravity models is proposed. In Ref. [59], the scenarios of nearly degenerate gaugino masses are considered. The pair production of light gluinos can have multitop final states [60] and multi-b final states [61], and it is expected that the multilepton and multi-b jet channels are sensitive to the light gluino mass region due to the clean SM background.

The lightest supersymmetric particle (LSP), like the neutralino, can be a cold dark matter candidate. The light gluino scenarios can also address the dark matter relic density in our Universe via the gluino-LSP coannihilation, which motivates us to examine such scenarios with current LHC data. Among them, as given in Ref. [58,62], the gluino-LSP coannihilation region is represented by points LG3-5. Such a scenario might lead to a long-lived gluino and chargino, which can have interesting LHC phenomenologies, like the displaced kink appearing in the detectors, as explored in Ref. [63] where the signature of a gluino

[1]In the NMSSM, the case that the heaviest *CP* event Higgs (H_3) might be the discovered Higgs boson has been explored in Refs. [30,31].

decaying to a wino-like LSP is considered. The long-lived charged wino can also be captured by the silicon tracker detectors at the ATLAS and CMS experiments. More recent work on the detection of gluino-LSP coannihilation can be found in Ref. [41], where the search for compressed SUSY by using a monojet signature has been carefully evaluated.

Light gluino scenarios accompanied by a light third generation of squarks have been the intense search focus at the LHC. According to the SUSY search results from the ATLAS [33] and CMS [32] Collaborations, the gluino mass has been excluded up to ~ 1.3 TeV with $m_{\tilde{q}} \simeq m_{\tilde{g}}$ in the CMSSM/mSUGRA. The upper limit reduces to ~750 GeV with decoupled squarks. If interpreted in simplified models, different decay patterns will be considered separately. For the 100% decay chain, $\tilde{g} \to t\bar{t}\tilde{\chi}_1^0$ (mediated by a virtual $\tilde{t}$), the allowed gluino mass has been pushed up to ~1.2 TeV for a LSP lighter than ~400 GeV, and ~750 GeV for all available LSP masses. As for the decay chain $\tilde{g} \to b\bar{b}\tilde{\chi}_1^0$ (mediated by a virtual $\tilde{b}$), $m_{\tilde{g}} \lesssim 1.2$ TeV has been ruled out with $m_{\tilde{\chi}_1^0} < 500$ GeV. A gluino lighter than ~1 TeV with $m_{\tilde{\chi}_1^0} \lesssim 400$ GeV is excluded in the non-b tagging analysis. Bounds for a long-lived $\tilde{g}$ which can form a R hadron are also available, where $m_{\tilde{g}} \lesssim 1$ TeV are excluded by using the signature of slow-moving objects (low β, $\beta\gamma$) in the detectors.

It should be noticed that all experimental bounds at the LHC are obtained by using some simple assumptions, where typically the decay branching fraction is oversimplified to be either vanishing or 100%. In reality, to evaluate whether these light gluino models are alive or dead, the model dependence must be carefully examined. For such a purpose, a more reliable approach is the Monte Carlo simulation, where model dependence can be correctly accounted for.

In this work, we focus on the bounds to light gluino scenarios in a concrete model—the NMSSM. To incorporate the direct search for SUSY, we assume that squarks of the first two generations are heavier than 1.5 TeV, while we allow the squarks of the third generation and gluino to be light. We explore two cases of interpretations for the Higgs boson data: (1) The lightest CP-even Higgs boson is around 125–127 GeV; (2) the second lightest CP-even Higgs boson is around 125–127 GeV.

We choose 2400 points or so to perform a detailed Monte Carlo simulation analysis, and we observe that the direct SUSY searches at the LHC impose a strong constraint on the light gluino scenarios represented by these points. We observe that the gluino-LSP coannihilation region in the natural SUSY models can bound the gluino mass up to 400 GeV, and the experiments can rule out points with gluino mass up to 1.0 TeV or so if the gluino dominantly goes to $t\bar{t}\tilde{\chi}_1^0$ and $b\bar{b}\tilde{\chi}_1^0$. The reason for this can be attributed to the fact that the coannihilation region demands that the gluino is around 300 GeV. But, due to its huge production rate, the bounds derived from the associated monojet process $pp \to j + \tilde{g}\,\tilde{g}$ and the α_T analysis approach require that the gluino mass should be larger than 400 GeV. It is interesting to note that the α_T analysis approach is also sensitive to the coannihilation region due to a relatively large fraction of boosted data samples in the signal events.

The paper is organized as follows. In Sec. II, we describe the Markov chain Monte Carlo method and our scanning strategy, as well as the experimental bounds, except the direct SUSY search bounds. In Sec. III, we tabulate the main direct SUSY search bounds considered in this work, describe our workflow, and present our main numerical analysis. In Sec. IV, we examine the constraints on the benchmark points proposed in the literature and propose a few new benchmark points for future LHC runs and future colliders. We end this paper with discussions and a conclusion.

II. SCANNING STRATEGY

A. The setup for scanning and the MCMC method

Specifically, we scan the parameter space of the natural NMSSM defined at the electroweak scale. The null search results of the signature of colored squarks at the LHC constrain the first two generation squark masses to be heavier than 1.5 TeV, which motivates us to set their mass parameters as follows:

$$M_{\tilde{Q}_{1,2}} = M_{\tilde{U}_{1,2}} = M_{\tilde{D}_{1,2}} = 1.5 \text{ TeV}. \tag{4}$$

Then we are left with a 15-dimensional parameter space (for the sake of simplicity, we fix $A_E = 0$) to be considered. To capture the typical features of natural SUSY and light gluino scenarios, we choose the range of these parameters as

$$\begin{aligned}
&0 < \lambda < 0.7, \quad 0 < |\kappa| < 0.7, \quad 1.1 < \tan\beta < 30, \quad 100 \text{ GeV} < \mu < 800 \text{ GeV},\\
&|A_\lambda| < 3 \text{ TeV}, \quad |A_\kappa| < 500 \text{ GeV}, \quad 100 \text{ GeV} < m_{Q_3}, m_{U_3} < 700 \text{ GeV},\\
&100 \text{ GeV} < m_{D_3} < 1000 \text{ GeV}, \quad |A_t| < 5 \text{ TeV}, \quad |A_b| < 3 \text{ TeV}, 10 \text{ GeV} < M_1 < 1 \text{ TeV},\\
&100 \text{ GeV} < M_2 < 1 \text{ TeV}, \quad 200 \text{ GeV} < M_3 < 1.3\text{TeV}, 100 \text{ GeV} < M_{\tilde{l}} = M_{\tilde{E}} < 500 \text{ GeV},
\end{aligned} \tag{5}$$

where λ and κ are dimensionless parameters in the superpotential given in Eq. (1). The parameter $\tan\beta = \frac{v_u}{v_d}$ is the ratio of the VEVs of H_u and H_d, and the μ term is defined as $\mu \equiv \lambda s$, where s is the VEV of singlet S. The mass parameters of the Higgs potential, m_{H_u}, m_{H_d}, and m_S, are not free parameters and can be expressed as the combinations of other free parameters from the minimization of the Higgs potential.

Obviously, it is very difficult to find the typical features of such parameter space since its dimensionality is too high to scan in a grid method or in a random scanning method. Supposing that we need 10 points in one-dimensional parameter space, then 10^{15} points at least are necessary for the current situation. To circumvent such an issue of computational cost, instead, we adopt the Markov chain Monte Carlo (MCMC) method [64] in our scanning.

The MCMC method is a sampling method to generate a chain of points of the parameter space with a density distribution consistent with experimental constraints. In this method, the computational time at its best performance is proportional to the dimensionality in a linear way, in contrast to the power way in the random scanning method. The MCMC method has been widely adopted in numerical analyses of many research fields, especially in astrophysics [65]. Recently, this method has also been applied in SUSY model scanning [66–69]. A more recent application and improvement of the MCMC method to take into account the constraints from the ATLAS and CMS collaborations can be found in [70].

The method is inspired by the Bayesian theorem, which can be written as below:

$$p(H|d) = \frac{p(d|H)p(H)}{p(d)} \tag{6}$$

where $p(H|d)$ is defined as the posterior probability of the hypothesis after taking into account experimental data. $p(d|H)$ is the sampling distribution of the data assuming the hypothesis is true. And if it is considered as a function of the hypothesis for fixed data, it is called the likelihood function. $p(H)$ is the prior probability which represents our state of knowledge before seeing the data. $p(d)$ is the marginal likelihood which is just a normalization factor in our case and will be ignored for now.

In this work, d and H denote a set of computed experimental observables in the model and a set of model parameters given in Eq. (5), respectively. $p(H|d)$ is the desired distribution in the parameter space of our scanning after taking into account all experimental constraints. $p(H)$ is taken as a flat distribution in this work, which is defined as

$$p(H) = \begin{cases} 1 & d_{min} < d < d_{max} \\ 0 & \text{otherwise.} \end{cases} \tag{7}$$

$p(d|H)$ denotes the likelihood function determined by experimental constraints, which is defined as

$$p(d|H) = \prod_i p(d_i|H), \tag{8}$$

where $p(d_i|H)$ denotes the likelihood function of each of the experimental constraints.

The main experimental constraints considered in this work are listed in Table I. When the Xenon100 results are applied in our scanning, the proton-DM scattering cross section is rescaled by the formula $\sigma_p^{SI} \times \Omega h^2/0.11$. And the likelihood functions $p(d_i|H)$ adopted in this work can be classified into three categories:

TABLE I. Physical bounds which have been taken into account in our scanning are listed here.

Experimental observables	Mean value	Deviation	Ref.
$BR(B^+ \to \tau^+\nu_\tau)$	1.67×10^{-4}	0.4×10^{-4}	[72]
$BR(B \to X_s\gamma)$	3.52×10^{-4}	0.3×10^{-4}	[73]
$BR(B_s \to \mu^+\mu^-) < 4.5 \times 10^{-9}$			[74]
$\Omega h^2 < 0.136$			[75]
Xenon100 (2012)			[76]
m_{Higgs}	125 GeV	2 GeV	
$R_{\gamma\gamma}$	1.6	0.4	[77,78]
R_{VV}	1.0	0.2	

(i) Exclusion bounds imposed by setting the likelihood to zero if the point is already excluded and to 1 if it is not excluded. For example, to impose a likelihood value for all theoretical points in our scanning, we assign a zero value to a point if it is unphysical or theoretically unacceptable. Here a point being unphysical or theoretically unacceptable has quite a few meanings: for example, up to the GUT scale Λ_{GUT}, the point might run into a Landau pole or be too big (say larger than 4 π) for some of its physics parameters at some energy scales below Λ_{GUT}, it might lead to an unphysical global minimum at the electroweak symmetry scale, it might have a spectrum with a tachyonic mass for a particle, it might have a spectrum for which the lightest neutralino is not a LSP, it might fail to reach a convergent two-loop renormalization group equations solution, or it might possess no electroweak symmetry breaking. The bounds of the Xenon100 and from the Tevatron and LEP on the masses of sparticles and the Higgs boson are realized in this way as well.

(ii) Upper bounds described by step functions:

$$p(d_i|H) = \frac{1}{1 + \exp[\frac{d_i[H] - d_{\text{upper}}}{0.01 d_{\text{upper}}}]}, \tag{9}$$

where $d_i[H]$ means the observable computed in the NMSSM. For example, the bound of dark matter relic density is realized by a step function. Although we also use a step function to the rare decay $B_s \to \mu^+\mu^-$, we notice that the LHCb Collaboration claimed a discovery of this mode with a measured branching fraction $3.2^{+1.5}_{-1.2} \times 10^{-9}$ [71]. Nonetheless, our main results are not sensitive to this bound.

(iii) Physics constraints described by Gaussian functions with well-measured central values and deviations,

$$p(d_i|H) = \exp\left[-\frac{(d_i[H] - d_{\text{cen}})^2}{\sigma^2}\right]. \tag{10}$$

For example, the likelihood function of the Higgs boson mass is taken as a Gaussian function with a central value 125 GeV, and an allowed deviation is taken as 2 GeV.

We would like to address the theoretical uncertainties given in Table I. The NMSSMtools package has assumed large theoretical uncertainties for FCNC B transition processes, some of which can be up to 100%. As explored in [79], the typical uncertainties in spectra of around 1% can lead to a deviation up to 10% in calculating relic density, especially for the regions where $\tan\beta$ or m_0 are large. In order to take into account these theoretical uncertainties, we have deliberately chosen relatively loose bounds for our sampling and have defined our parameter space to be far away from the regions where $\tan\beta$ or m_0 is large.

Once the likelihood function, which has incorporated all experimental constraints appropriately, has been specified, we can construct Markov chains through the Metropolis algorithm. The chain is a set of points in our parameter space, which can be labeled as $\{P_0, P_1, P_2, \ldots P_i, P_{i+1}\ldots\}$. We start with a seed (labeled as P_0). The chain can be generated by the following steps: (1) For any point P_i, $i = 0, 1, 2, \ldots$, we compute the value of the likelihood function $P(d|P_i)$. (2) A proposed point in our parameter space labeled as P_p is introduced, and the value of the likelihood function is evaluated as $P(d|P_p)$. If $P(d|P_p) > P(d|P_i)$, this walk is accepted and a new starting point is found, $P_{i+1} = P_p$. If $P(d|P_p) < P(d|P_i)$, this walk is accepted with a probability $P(d|P_p)/P(d|P_i)$. When this proposed step is accepted, we label it as $P_{i+1} = P_p$; when this proposed step is not accepted, the old point P_i will be used, i.e. $P_{i+1} = P_i$. (3) Repeat these two steps; after a long and sufficient walk (proportional to the dimensionality of parameter space, say 2.5 million for each case), a Markov chain with sample points reflecting the experimental constraints can be constructed.

As observed in [66], reducing the computational time while maintaining sufficient sample points which capture the features of the constrained parameter space can be balanced by utilizing an appropriate proposal step in each walk. According to the rule of thumb, a step with an acceptance rate around 25%–30% is the best one, which is realized in our scanning by trial and error.

With all these advantages of the MCMC method, we have to focus on getting past the typical shortcomings of this method, as pointed out in Refs. [80,81]. We have conducted the following examinations of our sampled points:

(i) To reduce the starting point bias in our scanning, we discard the first 100,000 steps of the MCMC (the so-called burn-in period). We have checked that a few different starting points yield the same final distributions so as to remove the starting point dependence of our sampled points.

(ii) Another issue is the length of the sampled chains: What is the right length for a chain which can sufficiently sample the parameter space? We use the convergence conditions of physical quantities. By examining the averaged $m_{\tilde{g}}$ and its variance, we have found that these quantities converge when using samples of 1,000,000 points and 1,250,000 points, for each chain. This indicates that our sampled points are converged, and a stationary distribution has been achieved.

(iii) There is an issue regarding how to sample the disconnected regions in the parameter space. For example, the constraint of the Higgs mass can lead to two disconnected regions: one with large positive A_t, the other with large negative A_t. To sample these two disconnected regions, we use two starting points with different signs of A_t in each of these two disconnected regions.

We are aware of the fact that our current usage of the MCMC method may not sample those well-motivated but isolated islands which could exist in the parameter space. But our main purpose is to examine how the direct LHC SUSY search can constrain the typical parameter space of the natural NMSSM defined in Eq. (5), especially the light gluino scenarios where the gluino dominantly decays to $t\tilde{t}$, $b\tilde{b}$, and $g\tilde{\chi}_1^0$, so we think the method used here is sufficient for us to extract some representative information on the theoretical parameter space allowed by experiments.

B. Features of the sampled points

In our scanning, we consider two cases of the interpretations for the Higgs boson data: In the first case, we assume that H_1 is the SM-like Higgs boson; in the second case, we assume that H_2 is the SM-like Higgs boson. We implement the MCMC method in NMSSMtools 3.2.1 [82,83] and construct eight chains with 10 million points in total (5 million points for each case with $\kappa > 0$ and $\kappa < 0$). The distribution of mass spectra of sparticles for both the first case and the second case is shown in Fig. 1.

There are a few comments on Fig. 1in order:

(i) For the Higgs sector, in the first case, the mass of H_2 can spread in a quite large range from 120 GeV up to 600 GeV. Similarly H_3, A_2 and $H^\pm$ are quite heavy and also expand in a large range from 400 GeV up to 1600 GeV. In contrast, in the second case, the mass of H_1 is confined to be smaller than H_2, and H_3, A_2 and $H^\pm$ tend to be heavier than 1000 GeV.

(ii) For the neutralino sector, in the first case, the lightest neutralino can spread from a few GeV to 340 GeV, and most of them are lighter than 200 GeV. The second and third neutralinos can expand from a few tens of GeV to 700 GeV. In contrast, in the second case, the LSP is compressed in a much smaller mass range from a few GeV to 220 GeV, while most of them are situated near

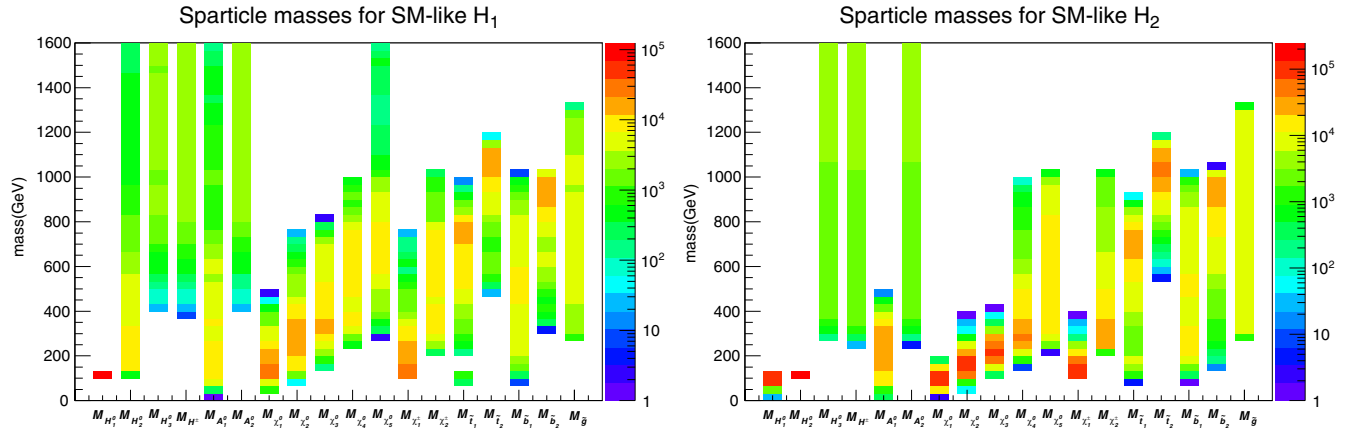

FIG. 1 (color online). The distributions of mass spectra of sparticles are shown for the first and second cases.

100 GeV. The second and third neutralinos are also compressed in much smaller ranges.

(iii) For the chargino sector, in the first case, the lighter chargino can expand from 100 GeV to 700 GeV. In contrast, the lighter chargino can only expand from 100 GeV to 400 GeV in the second case.

(iv) It is interesting to notice that the distribution of stop squarks, sbottom squarks and gluinos is similar in both cases. It is remarkable that in the second case, the points representing the gluino-LSP coannihilation region have not yet been found, while for the first case, there are quite a lot of points being sampled in such a region.

We also show the features of these points when projected on the $m_{\tilde{t}_1} - m_{\tilde{\chi}_1^0}$ plane, the $m_{\tilde{b}_1} - m_{\tilde{\chi}_1^0}$ plane, and the $m_{\tilde{g}} - m_{\tilde{\chi}_1^0}$ plane, as shown in Figs. 2–4. One feature shown in Figs. 2–4 is that the favored mass of the LSP is around 100 GeV for both cases. In the first case, the LSP is Bino or Wino dominant and its mass is determined by parameters M_1 and M_2, which is similar to the case of the MSSM. In the second case, the LSP is either Higgsino or singlino dominant and its mass range is determined by μ, λ, κ, etc.

From Fig. 2, we can see that both cases favor a relatively heavy $\tilde{t}_1$ (say, around 750 GeV in the first case and 700 GeV in the second case); such a tendency is determined by the Higgs boson mass.

It is observed that the second case allows a narrower LSP mass range than the first case. When $\kappa > 0$, such a feature can be analytically understood by a correlation between the singlet scalar mass and the singlino mass. Their mass formulas are provided below:

$$M_{H,S}^2 = \lambda^2 v^2 A_\lambda \frac{\sin 2\beta}{2\mu} + 4\kappa^2 s^2 + A_\kappa \kappa s, \tag{11}$$

$$M_{\tilde{S}} = 2\ \kappa s. \tag{12}$$

In the second case, it is required that the lightest Higgs boson be mainly singletlike, which will set an upper limit for $M_{H,S} \lesssim 125$ GeV. To guarantee that the second Higgs boson mass is $m_{H_2} \sim 125$ GeV, a cancellation condition given below,

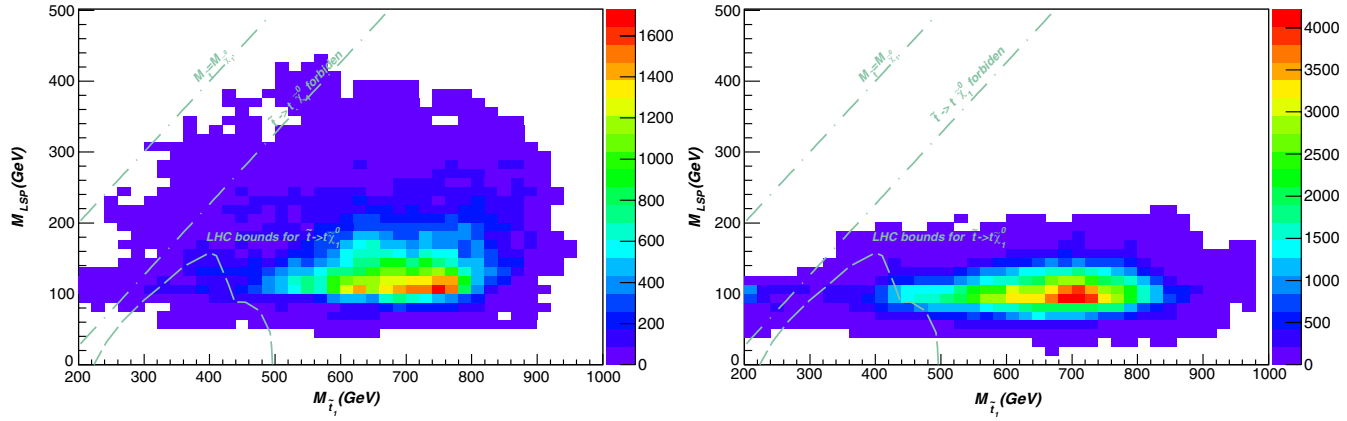

FIG. 2 (color online). The distribution of points in the $m_{\tilde{t}_1} - m_{\tilde{\chi}_1^0}$ plane is shown for the first and second cases.

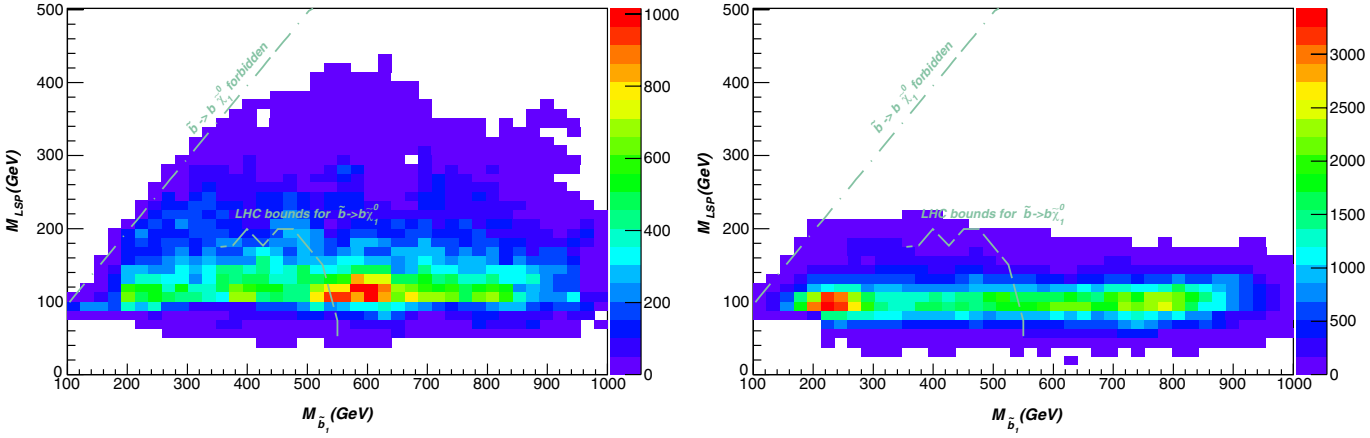

FIG. 3 (color online). The distribution of points in the $m_{\tilde{b}_1} - m_{\tilde{\chi}_1^0}$ plane are shown for the first and second cases.

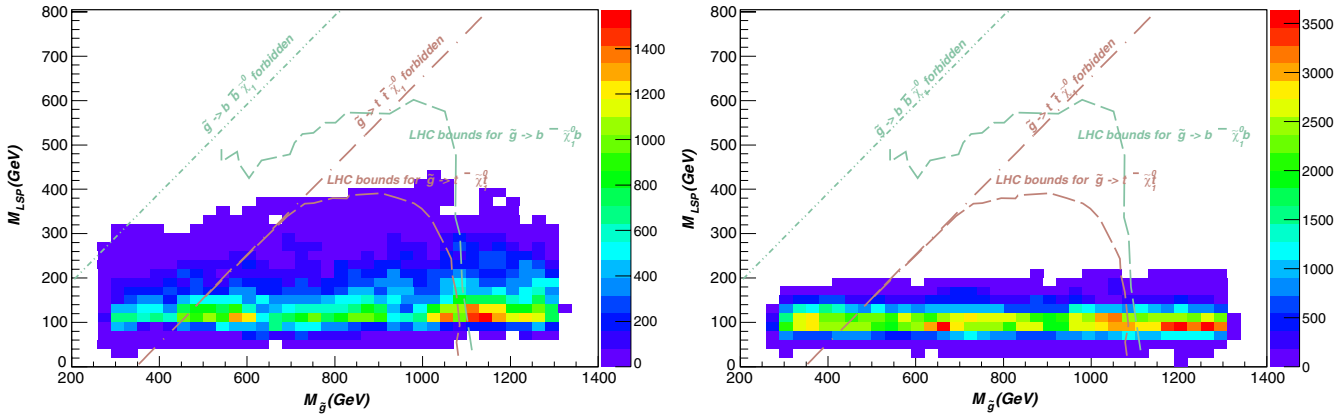

FIG. 4 (color online). The distribution of points in the $m_{\tilde{g}_1} - m_{\tilde{\chi}_1^0}$ plane are shown for the first and second cases.

$$1 - (A_\lambda/2\mu + \kappa/\lambda)\sin 2\beta \simeq 0, \tag{13}$$

is needed, as pointed out in [13]. With these conditions, after some linear algebra, we can solve $s_{\max}$, which is given as

$$|\kappa s|_{\max} = \frac{1}{8}\left(|A_\kappa| + \sqrt{500^2 + A_\kappa^2 - 16\lambda^2 v^2\left(1 - \frac{\kappa \sin 2\beta}{\lambda}\right)}\right). \tag{14}$$

Since $(1 - \frac{\kappa \sin 2\beta}{\lambda}) > 0$ and most $|A_\kappa|$ cannot be larger than 300 GeV in our scanning (after imposing all experimental cuts), $\kappa s_{\max}$ should be smaller than 110 GeV. The only exception occurs when $M_{H,S} \lesssim 125$ GeV due to the large mixing between the singlet and the doublet H_d. Then the singlet can have a mass $M_{H,S} > 125$ GeV and become lighter than 125 GeV after a large mixing with H_d. However, this kind of space needs a certain degree of fine-tuning.

Moreover, another way to understand such a feature is we need a relatively small μ_{eff} (∼100–200 GeV) to produce an appropriate singlet-doublet mixing which is required by the 125 GeV SM-like Higgs boson mass. Consequently, we have $M_{\tilde{s}} = 2\,\kappa s = 2\frac{\kappa}{\lambda}\mu \lesssim \mu$, which results in a light LSP within a narrower range. We observe that such a feature also holds even when $\kappa < 0$.

In contrast, for the first case, the LSP is Bino or Wino dominant; its mass range is simply determined by the range of parameters M_1 and M_2, and there is no such correlation. As shown in Fig. 2, in the first case, the points in the stop-LSP coannihilation region can easily be found, while in the second case, such points have not been found.

In Fig. 3, it is obvious that the first case allows a wider region for the sbottom-neutralino coannihilation. Moreover, the Higgs boson mass does not affect the distribution of mass of $\tilde{b}_1$, since the contribution of $\tilde{b}_1$ to the Higgs boson mass is much smaller when compared with that of $\tilde{t}_1$ if $\tan\beta < 30$.

In Fig. 4, we see that since the gluino can contribute to the Higgs boson mass via two loops, the mass of the gluino can be affected by the Higgs boson data. The most favored gluino masses are around 1.1 TeV and 1.2 TeV for the two cases, respectively.

To appreciate how stringent the LHC bounds can be, in Figs. 2–4, we deliberately show the combined LHC bounds derived from the simplified models. In these figures, we combine the available bounds from both the ATLAS and CMS collaborations [84]. In Fig. 2, we use the bounds of $pp \to \tilde{t}\,\tilde{t}$ with $\tilde{t} \to t\tilde{\chi}_1^0$ from the ATLAS analysis based on the data set of 4.7 fb^{-1} and $\sqrt{s} = 7$ TeV. In Fig. 3, we adopt the bounds of $pp \to \tilde{b}\,\tilde{b}$ with $\tilde{b} \to b\tilde{\chi}_1^0$ from the CMS analysis based on the data set of 4.98 fb^{-1} and $\sqrt{s} =$ 7 TeV by using the α_T variable. In Fig. 4, we compile two types of bounds: (1) $pp \to \tilde{g}\,\tilde{g}$ with $\tilde{g} \to t\bar{t}\tilde{\chi}_1^0$ from the ATLAS Collaboration based on the data set of 5.8 fb^{-1} and $\sqrt{s} = 8$ TeV and (2) $\tilde{g} \to b\bar{b}\tilde{\chi}_1^0$ from the CMS Collaboration based on the data set of 4.98 fb^{-1} and $\sqrt{s} = 7$ TeV.

One obvious concern is whether all those allowed points within the bound curves are still alive or whether all points outside the bound curves are safe. To address this question, we sample around 2400 of the 10 million points (including both interpretations of the Higgs boson data) to perform an analysis of the constraints from the direct SUSY searches by the LHC experiments. Because of our limited computing resources, we only choose around 2400 points to conduct the detailed Monte Carlo studies, where it takes more than 5 hours for each point to generate all the relevant MC events for both the $\sqrt{s} = 7$ TeV and $\sqrt{s} = 8$ TeV cases (around 500 k for each point). Anyhow, the sparticles masses distributions are similar between these 2400 points and those 10 million points, especially for the gluino, the lightest neutralino, and the third generation squarks. Therefore, the analysis of these 2400 points might be representative of the sampled 10 million points. Nevertheless, to correctly interpret our results, the readers must be aware that our conclusions are based on these 2400 points generated by the MCMC method. And our conclusions might not hold for isolated islands in the parameter space, which may not have been well sampled in this study.

III. CONSTRAINTS FROM DIRECT SUSY SEARCHES AT THE LHC

A. SUSY search bounds from LHC experiments

To study the constraints from the direct SUSY searches by the LHC Collaboration, we implement in our analysis results from both the ATLAS and CMS collaborations for the data sets accumulated with the collision energies $\sqrt{s} = 7$ TeV and $\sqrt{s} = 8$ TeV, shown in Table II, where the direct SUSY search channels from both the ATLAS and CMS collaborations and the references are tabulated. Below we briefly describe these search channels and their sensitivity to possible SUSY signals.

(i) The jets $+ \not{E}_T$ channel is the classical search channel for the signature of pair production of squarks and gluino. In this search channel, a large H_T (defined as the scalar sum of p_T of all reconstructed jets in one event) and a large missing transverse energy (denoted as $\not{E}_T$) are required. The hard H_T is expected if all jets are produced from the heavy SUSY particle decay. And a large $\not{E}_T$ predicted in R-parity conserving SUSY can efficiently suppress QCD background.

TABLE II. The direct SUSY search results from the ATLAS and CMS collaborations are tabulated, where the superscript * in the channels denotes the results obtained from the data set with the collision energy $\sqrt{s} = 8$ TeV.

Channels	ATLAS	CMS
jets $+ \not{E}_T$	[85–90], [126]*	[130]
multijets $+ \not{E}_T$	[91,92], [127]*	[131]
B jets + jets $+ \not{E}_T$	[93–98]	[132], [138]*
B jets + leptons + jets $+ \not{E}_T$	[99–103]	[133], [139]*
leptons + jets $+ \not{E}_T$	[104–117], [128,129][8]	[134]
multileptons $+ \not{E}_T$	[118–124]	[135]
Z boson + jets $+ \not{E}_T$		[136]
Monojet $+ \not{E}_T$	[125]	[137]

Apart from these two simple cuts, some characteristic kinematic variables, such as the α_T variable, the M_{T2} variable, and the Razor variable, are used to discriminate SUSY signal from the SM background. Below we describe these kinematic variables in order.

As introduced in [140], the kinematic variable α_T is designed to distinguish the real $\not{E}_T$ from the hard process and the pseudo-$\not{E}_T$ from mismeasurement of the jet. It is defined as

$$\alpha_T = \frac{E_T^{j_2}}{M_T},$$
$$M_T = \sqrt{\left(\sum_{i=1}^{2} E_T^{j_i}\right)^2 - \left(\sum_{i=1}^{2} p_x^{j_i}\right)^2 - \left(\sum_{i=1}^{2} p_y^{j_i}\right)^2} \qquad (15)$$

for any two-jet final state (a multijet final state can be regrouped into a two-jet final state by using the combination algorithm that minimizes the E_T difference between the two pseudojets [141]), where E_T^{j2} denotes the $\not{E}_T$ of a less energetic jet. An $\not{E}_T$ from SUSY particle decay favors a α_T with values greater than 0.5, while an $\not{E}_T$ from the mismeasurement of jet energy typically leads to a α_T with values smaller than 0.5.

The kink variable M_{T2} is introduced in [142]; it is supposed to determine the transverse mass of a new particle from its pair production, with each particle decaying to a visible daughter and an invisible one. It is expected that two reconstructed transverse masses of each particle in each event should be the same or close to each other. Similar to the α_T variable, a multijet final state can be regrouped into

a two-jet final state by using the hemisphere algorithm. Typically, SUSY signals can have a larger M_{T2} around several hundred GeV, while the background of the SM favors a smaller M_{T2}.

The Razor variable is introduced in [143]; it is defined by the CMS Collaboration as

$$R \equiv \frac{M_T^R}{M_R}, \tag{16}$$

where M_T^R and M_R are defined as

$$M_R \equiv \sqrt{(E_{j1}+E_{j2})^2-(p_z^{j1}+p_z^{j2})^2}, \tag{17}$$

$$M_T^R \equiv \sqrt{\frac{E_T(p_T^{j1}+p_T^{j2})-\vec{E}_T\cdot(\vec{p}_T^{j1}+\vec{p}_T^{j2})}{2}}, \tag{18}$$

respectively. This variable has been used to search for SUSY signals with colored sparticles in pair production and decaying into invisible particles and jets. Signal events are characterized by a large M_R and a large R (which peaks at around 0.5, while QCD multijet background events peak at around zero). In this study, we have not taken into account the bounds obtained from the Razor approach, which will be included in our future work.

(ii) The multijets $+ \not{E}_T$ channel is well motivated by the signals of light squarks of the third generation and signals of gluinos decaying to squarks of the third generation. Typically, such a signal can lead to more energetic jets, when compared with the signal of squarks of the first two generations. For example, the signal from $pp \to \tilde{g}\tilde{g} \to (t\bar{t}\tilde{\chi}_1^0)(t\bar{t}\tilde{\chi}_1^0)$ with hadronic top quark decays can yield many jets in the final state. This search channel should be sensitive to such types of signals.

(iii) The $B-$jets $+$ jets $+ \not{E}_T$ channel can utilize the b-tagging technique, which can be very powerful to reject the QCD background. This search channel can improve the sensitivity to signals of third-family squark production and signals of gluino pair production with gluinos decaying to the third generation squarks (both on shell and off shell), which can produce many b jets in the final states.

(iv) The B-jets $+$ leptons $+$ jets $+ \not{E}_T$ channel can utilize both the b-tagging technique and the lepton(s) (single or two same-sign dileptons) and can reliably suppress the huge QCD background. It is supposed to be sensitive to the signal of four top final states from gluino pair production with $\tilde{g} \to t\bar{t} + \not{E}_T$ and $pp \to \tilde{t}\tilde{t} \to t\bar{t} + \not{E}_T$.

(v) The leptons $+$ jets $+ \not{E}_T$ channel can utilize the high efficiency of lepton identification and significantly reject the QCD background. One single lepton, opposite-sign dilepton and same-sign dilepton channels have been considered by experimental collaborations. The channel is expected to be sensitive to $pp \to \tilde{t}_1\tilde{t}_1$ and multitop final states.

(vi) For the multileptons $+ \not{E}_T$ search channel, three or more well-isolated leptons are required. The trilepton channel would be an ideal channel to explore chargino and neutralino pair production, decaying to the LSP and leptons mediated by sleptons. In our scanned parameter regions, we observe that the chargino and neutralino can be very light, as shown in Fig. 1. Consequently, their production rate can be very large and should be considered.

(vii) The Z-boson $+$ jets $+ \not{E}_T$ search channel is supposed to utilize two isolated leptons from a Z-boson decay. The momenta, sign and flavor of each lepton can be measured quite well. The Z-boson peak can be reliably reconstructed. This channel is designed to explore the topology with the Z boson produced through a neutralino decaying in the cascade decay of colored sparticles.

(viii) The monojet search channel focuses on one single energetic jet originating from the initial-state radiation. Typically, the p_T of the jet is required to be larger than $\sim$100 GeV, and a large missing energy ($\not{E}_T > 200$ GeV) is required. This search channel can be sensitive to those coannihilation scenarios where the next to lightest supersymmetric particles is almost degenerate with the LSP.

The ATLAS Collaboration has provided upper limits for new physics, and we use those upper limits directly. Similar upper limits are missing in the documents of the CMS Collaboration. To extract these upper limits from the CMS Collaboration, we use the method proposed in [144,145] by assuming there is a 30% uncertainty on the possible new physics signal.

B. SUSY experimental bounds implemented

Below we will outline the main procedure for how to implement the SUSY experimental bounds in our study.

For each point selected from the constructed Markov chains, we use the NMSSMtools3.2.1 [82,83] to generate its mass spectrum and decay tables in Supersymmetry Les Houches Accord format. The mass spectra are used to evaluate the cross sections of the SUSY signals. For all points in our work, the most important processes include $pp \to \tilde{g}\tilde{g}$, $pp \to \tilde{t}_1\tilde{t}_1$, $pp \to \tilde{b}_1\tilde{b}_1$[2], $pp \to \tilde{\chi}_i\tilde{\chi}_j$ (where $\tilde{\chi}_i$ include both neutralinos and charginos) pair production. We typically notice that the cross sections

[2]We have taken into account the contribution of the process $pp \to \tilde{b}_2\tilde{b}_2$ and have found that the LHC bounds start to constrain those cases with $M_{\tilde{b}_2} < 600$ GeV.

of $pp \to \tilde{\chi}_i^0 \tilde{\chi}_j^0$, $pp \to \tilde{\chi}_i^\pm \tilde{\chi}_j^0$, $pp \to \tilde{\chi}_i^\pm \tilde{\chi}_j^\mp$ can be significantly large due to their small masses, like in the second case.

The next to leading order (NLO) cross section is evaluated by using the package prospino2 [146], which will be used to normalize the number of signal events in our analysis. Then, the mass spectra and decay tables are passed to the package MadGraph5 [147], and signal events with up to two additional radiative jets for the processes $pp \to \tilde{g}\tilde{g}$, $pp \to \tilde{t}_1\tilde{t}_1$, $pp \to \tilde{b}_1\tilde{b}_1$, $pp \to \tilde{\chi}_i\tilde{\chi}_j$ are generated. To avoid double counting in the matrix element calculation and the parton shower simulation, we adopt the MLM-matching scheme with the variable xqcut $= 100$ GeV. Then Pythia6 [148] is used to decay the sparticles to the particles of the SM at parton level and to simulate a parton shower and hadronization. We use PGS4 [149] to implement fast detector simulation. To reconstruct jets in the final objects, we adopt the anti-k_T jet algorithm with the cone size parameter $R = 0.5$, and assume the b-tag efficiency to be 60% in accordance with a mistagged rate for charm quark jets of 10% and for other light quark jets of 1%, respectively.

We generate 50,000 events for each of the signal processes at the parton level; after matching, typically we arrive at 30,000 matched events or more. The matched events will be passed to our SUSY bound analysis package to evaluate how many events can survive after implementing all experimental cuts.

To analyze the bounds imposed by the direct SUSY search at the LHC, we develop a systematic analysis package. The main goal of the package is to implement the SUSY constraints given by the ATLAS and CMS collaborations in simplified way. With the help of our package, we can evaluate whether a model is still alive or has been ruled out. Up to now, the searches that we have implemented are given in Table II, and we are upgrading our package by including new LHC bounds released recently.

For each search channel, by feeding the matched events of signal processes to our package, we can give the selection efficiency for each signal region. This selection efficiency is finally translated into the observed number of signal events in each signal region after cross sections and luminosity are taken into account. In order to perform an analysis similar to the LHC Collaboration, for each point we generate two independent event samples with the collision energies $\sqrt{s} = 7$ TeV and $\sqrt{s} = 8$ TeV, respectively.

In this work, the exclusion limits up to the observed 95% confidence level for each search channel in each signal region have been applied. Accordingly, we define the ratio $R = \frac{N_{\text{signal number}}}{N_{\text{observed limit}}}$ for each signal region in each search channel. To derive the most stringent constraint, we choose the maximal value of R among all search channels at all signal regions. Obviously, for a model in a specific search channel and a specific signal region, the ratio R is greater than 1, and this means that it has been ruled out by experiments

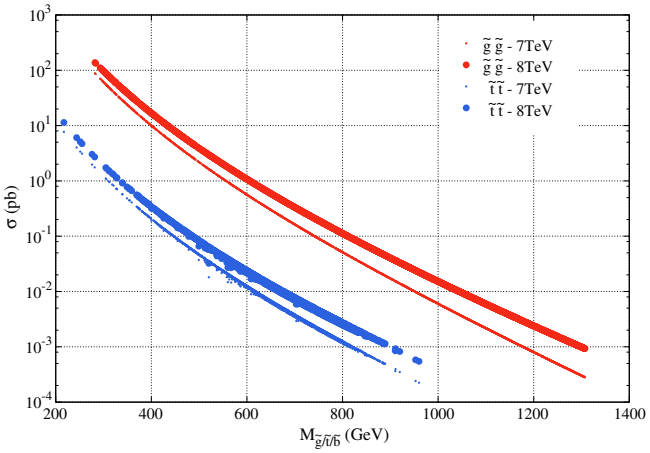

FIG. 5 (color online). The cross sections varying with the mass of the gluino and stop are shown here. The cross section of the sbottom is similar to that of the stop and is omitted.

(although we have not taken errors into account, neither Monte Carlo errors nor the fast detector simulation errors). Our package yields all Rs of each signal region in each search channel. By comparing the Rs, we can find the strongest bound, which is denoted by R_{max}.

C. Numerical analysis

Here we present our main results of the numerical analysis. In Fig. 5, we present the cross sections of the gluino and stop in our scanning. We highlight two observations: (1) Roughly speaking, the cross sections of the stop and gluino increase by a factor 2 when the collision energy increases from 7 TeV to 8 TeV; (2) when the stop and gluino have the same mass, the cross section of the gluino is 50 times larger than that of the stop. We also notice that the cross sections are almost equal for the stop pair production and the gluino pair production if the mass of $m_{\tilde{t}} \approx m_{\tilde{g}} - 250$ when $m_{\tilde{g}} = 600$ GeV and $m_{\tilde{t}} \approx m_{\tilde{g}} - 400$ GeV when $m_{\tilde{g}} = 1200$ GeV. At the tree level, the cross sections of $pp \to \tilde{t}\tilde{t}$ and $pp \to \tilde{g}\tilde{g}$ are simply determined by the mass parameters, while at the NLO level, colored sparticles at loop level can contribute and lead to a minor change in the cross section. We notice that the fluctuation in the cross section of the process $pp \to \tilde{t}\tilde{t}$ near the mass region 500–600 GeV, by a few points, originates from the stop-decay threshold ($m_{\tilde{t}} = m_t + m_{\tilde{g}}$) effect [150,151]. The cross section of $pp \to \tilde{b}\tilde{b}$ is similar to that of $pp \to \tilde{t}\tilde{t}$. Therefore, we neglect them in Fig. 5.

In Fig. 6, we first examine the constraints on the signal of either the process $pp \to \tilde{t}_1\tilde{t}_1$ or the process $pp \to \tilde{b}_1\tilde{b}_1$ in the $m - m_{\tilde{\chi}_1^0}$ plane, as shown in the right plot and in the left plot, respectively. The experimental bounds are the same as shown in Fig. 2. The $R_{\text{max}}(\tilde{t}\tilde{t})$ or $R_{\text{max}}(\tilde{b}\tilde{b})$ is obtained by using all kinds of SUSY search analysis approaches (including both α_T and M_{T2}, etc.).

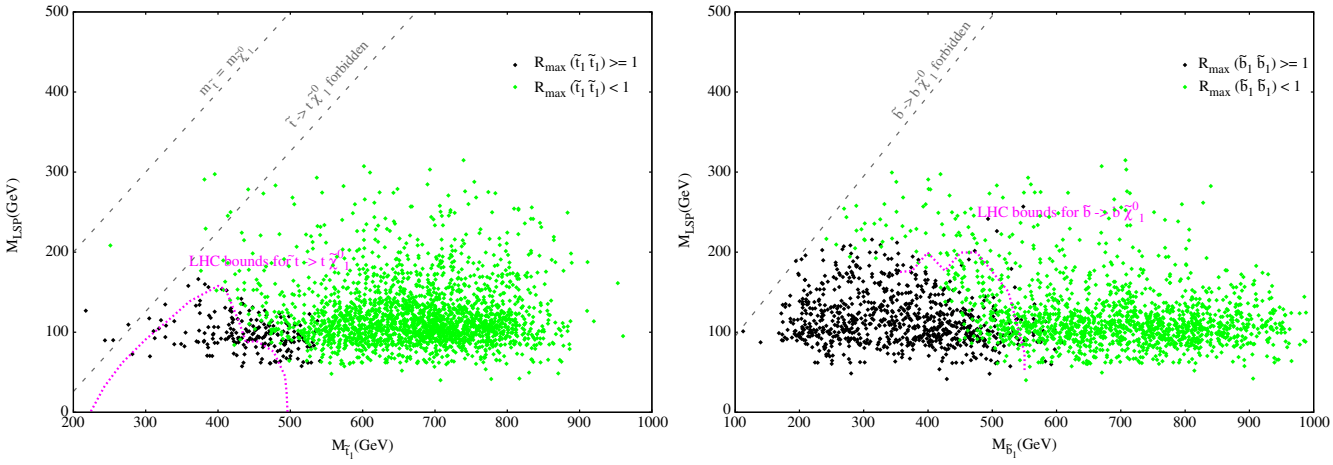

FIG. 6 (color online). The constraints to the solitary signal of $pp \to \tilde{t}_1\tilde{t}_1$ and $pp \to \tilde{b}_1\tilde{b}_1$ are demonstrated. $R_{\max}(\tilde{t}\,\tilde{t})$ [$R_{\max}(\tilde{b}\,\tilde{b})$] means the largest R values in all search channels, while the signature only includes the process $pp \to \tilde{t}_1\tilde{t}_1$ ($pp \to \tilde{b}_1\tilde{b}_1$).

It is interesting to notice that the green points inside the bound curves simply indicate that the branching fraction is too small and yields too few signal events to be meaningfully constrained. The black points outside the bound curves are found to be constrained by other search channels not deliberately designed for either the signal of $pp \to \tilde{t}_1\tilde{t}_1$ or the signal of $pp \to \tilde{b}_1\tilde{b}_1$. For example, the black points outside the bound curve near the point [500, 100] in the $m_{\tilde{t}} - m_{\tilde{\chi}^0_1}$ plane and those near the point [600, 100] in the $m_{\tilde{b}} - m_{\tilde{\chi}^0_1}$ plane are ruled out by the jet (M_{T2}) search channel, while several points near the region of point [500, 250] (with $\tilde{b} \to b\tilde{\chi}^0_i$, $\tilde{\chi}^0_i \to \tilde{l}l$, and a slepton decaying to a lepton and a LSP) are constrained by the two same sign leptons (2SSL) search channel. These black points outside the experimental bound curves clearly demonstrate the importance and necessity of a comprehensive analysis for a given model.

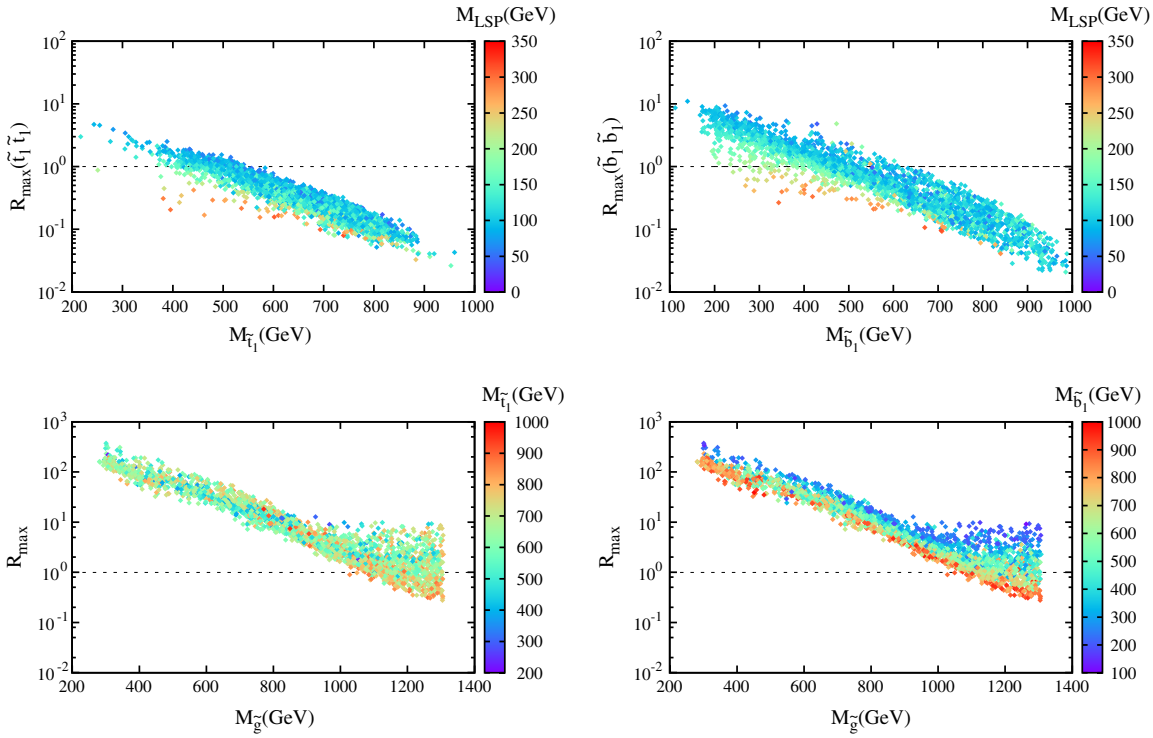

FIG. 7 (color online). In the upper row, the bounds for the stop and the sbottom are examined, where the signals are assumed to be $pp \to \tilde{t}_1\tilde{t}_1$ and $pp \to \tilde{b}_1\tilde{b}_1$, respectively. The y axis is $R_{\max}$, and the x axis is the mass of the stop and the sbottom, respectively. In the lower row, the bounds for all signals (including $pp \to \tilde{t}_1\tilde{t}_1$, $pp \to \tilde{b}_1\tilde{b}_1$, and $pp \to \tilde{g}\,\tilde{g}$) are taken into account. The x axis is the mass of the gluino, the y axis the $R_{\max}$, and the color bar indicates the mass of the stop and the sbottom, respectively.

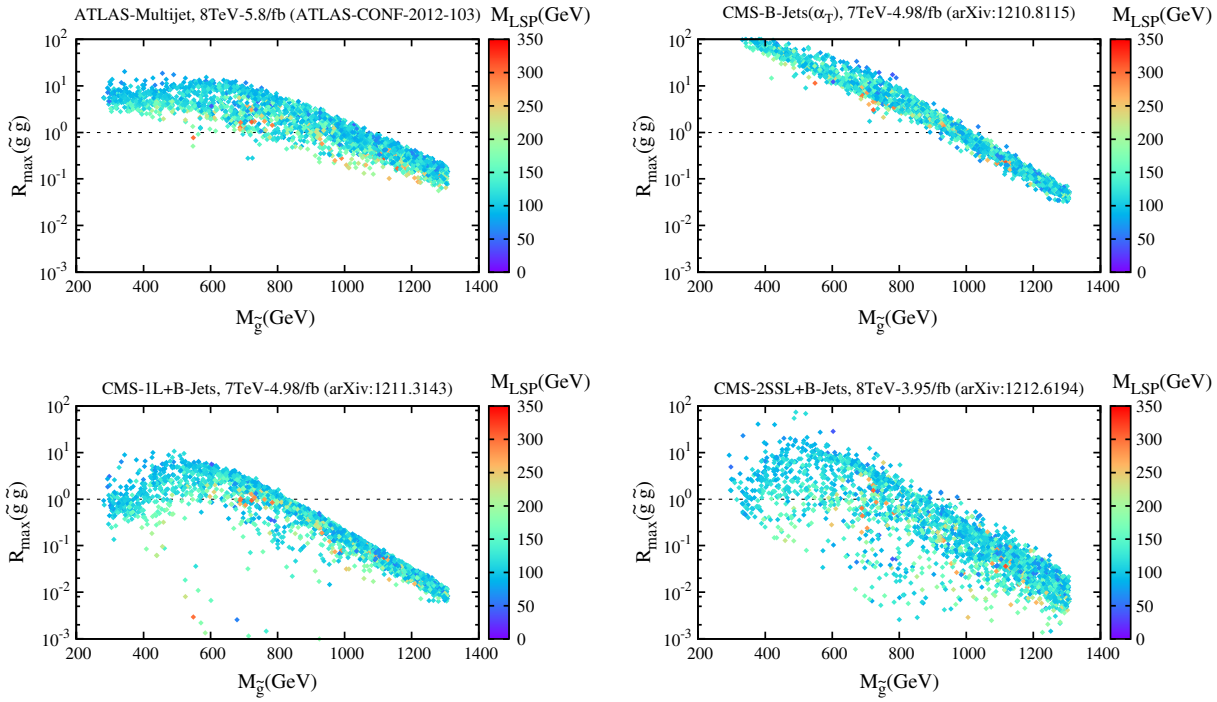

FIG. 8 (color online). Four channels for the signals from $pp \to \tilde{g}\,\tilde{g}$ are shown. The x axis is the gluino mass, while the color scale denotes the mass of the LSP.

Comparing with the results given in [20,152], we observe that when more experimental constraints up to 5 fb^{-1} with $\sqrt{s} = 7$ TeV and part of those from the analysis with $\sqrt{s} = 8$ TeV are included, the bounds to the stop and the sbottom have been improved, as clearly demonstrated by the scattering plots in the upper row of Fig. 7. It is straightforward to find that the stop mass can be excluded up to 550 GeV or so, while the sbottom mass can be excluded up to 600 GeV or so.

In Fig. 7, we show the bounds for the stop, sbottom and gluino. In the lower row, we show bounds against the gluino mass. We observe that most of the points have been ruled out or disfavored even if they cannot be constrained meaningfully by the signature of $pp \to \tilde{t}_1\tilde{t}_1$ or by the signal of the process $pp \to \tilde{b}_1\tilde{b}_1$. When the gluino is light, say less than 800 GeV, the most stringent bound is from the signatures of $pp \to \tilde{g}\,\tilde{g}$ due to its large cross section, and the bounds show a universal model dependence, which is indicated by the width of the band. The width of the band when $m_{\tilde{g}} < 800$ GeV is around 10; i.e. the sensitivity to the signature of a given $m_{\tilde{g}}$ can differ by a factor of 10. In contrast, the sensitivity of the signature of $pp \to \tilde{b}_1\tilde{b}_1$ can differ even more.

Comparing the left and right plots in the lower row, we observe that the bounds have a strong correlation with the sbottom mass. This correlation, especially at the right corner with 1 TeV $< m_{\tilde{g}} <$ 1.3 TeV where lots of points with a heavy gluino have been excluded, can be attributed to the fact that when the cross section $pp \to \tilde{g}\,\tilde{g}$ is much less than that of $pp \to \tilde{b}_1\tilde{b}_1$, consequently the real meaningful constraint is actually from $pp \to \tilde{b}_1\tilde{b}_1$. However, such a correlation with the stop mass is weak. The width of the band near the region 1 TeV $< m_{\tilde{g}} <$ 1.3 TeV becomes broader, since it is determined by the signature of $pp \to \tilde{b}_1\tilde{b}_1$, instead of $pp \to \tilde{g}\,\tilde{g}$.

In Fig. 8, we show four representative constraints on the gluino signals from different analysis approaches, which are supposed to be sensitive to the signature of the production process $pp \to \tilde{g}\,\tilde{g} \to t\bar{t}t\bar{t}\not{E}_T$, for instance. In the upper left plot, the bound from the multijet analysis approach is demonstrated, which can exclude the signals of most models with gluino mass lighter than 600 GeV. In the upper right plot, the bound from the B-jet plus α_T analysis can exclude the signals below 900 GeV. Meanwhile, this analysis approach enjoys less model dependence than the multijet analysis approach, as indicated by the width of the band formed by the points.

In the lower left plot, the bound from one lepton plus B jet plus $\not{E}_T$ is shown, and the meaningful constraints can reach up to 800 GeV. At the lower left corner of this plot, there are some points that cannot be constrained due to the small branching fraction of $\tilde{g} \to t\bar{t} + \not{E}_T$, and the dominant branching fraction is $\tilde{g} \to b\bar{b} + \not{E}_T$ or $\tilde{g} \to g + \not{E}_T$, while in the lower right plot, the bound from the same-sign lepton is demonstrated and the meaningful constraint can reach up to 800 GeV or so. Obviously, both of these channels rely upon the branching fraction of $\tilde{g} \to t\bar{t} + \not{E}_T$. Although the same-sign lepton mode is clean and has a very tiny SM

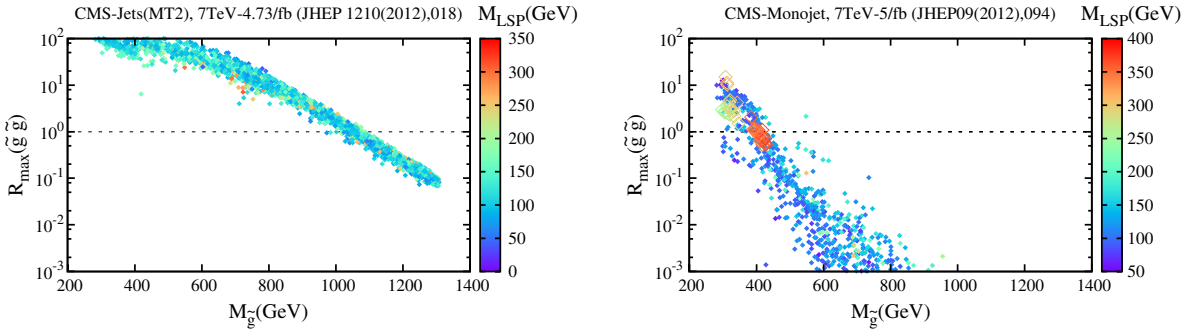

FIG. 9 (color online). The constraints from the M_{T2} analysis approach and the monojet channel are demonstrated, respectively. In the right plot, extra points of the gluino-LSP coannihilation are displayed by the empty diamonds.

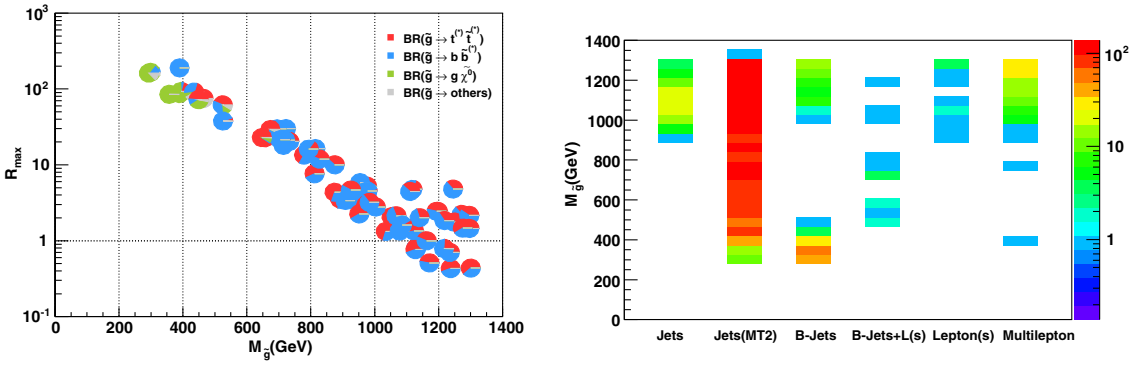

FIG. 10 (color online). In the left plot, the branching fraction dependence is examined by choosing 50 representative points. In the right plot, we show the statistics of how many models are excluded by which channels.

background, its sensitivity is similar to or worse than the search channel of one lepton + B jet + $\not{E}_T$ due to its much smaller branching fraction.

Among these four search channels, it is worth remarking that the bounds from the α_T analysis approach with b tagging is the most stringent and the least model dependent.

We also notice that, similar to the α_T approach, the M_{T2} approach also enjoys good sensitivity and model independence, as shown in the left plot of Fig. 9, where both the constraints from the M_{T2} approach and the constraints from the monojet plus $\not{E}_T$ channel are shown. We notice that the M_{T2} approach can achieve a sensitivity better than the α_T approach for most points, as revealed by the statistics shown in the right plot of Fig. 10.

Meanwhile, the monojet search channel alone can probe the gluino mass up to 400 GeV, as shown in the right plot of Fig. 9. To show the constraint of the monojet on the gluino-LSP coannihilation scenarios, we deliberately introduce 200 extra points in this plot, as denoted by the empty diamonds.

In the left plot of Fig. 10, 50 representative points with branching fractions denoted by pie charts are shown to demonstrate the effects of branching fractions of the four main decay chains (say $\tilde{g} \to t\bar{t}\not{E}_T$, $\tilde{g} \to b\bar{b}\not{E}_T$, $\tilde{g} \to g\not{E}_T$, and others). For each category of decay modes, we sum all on-shell or off-shell decay modes into one. For example, $\tilde{g} \to t^{(*)}\tilde{t}^{(*)}$ means that we count either the on-shell or off-shell decay modes of $\tilde{g} \to t\tilde{t}$, $\tilde{g} \to t^*\tilde{t}$, $\tilde{g} \to t\tilde{t}^*$, $\tilde{g} \to t^*\tilde{t}^*$, and sum over all allowed decay modes, while $\tilde{g} \to b\tilde{b}^{(*)}$ means either the on-shell or off-shell decay modes of $\tilde{g} \to b\tilde{b}$ and $\tilde{g} \to b\tilde{b}^*$.

We notice that the most stringent bounds of the gluino with mass lower than 1000 GeV depend upon the branching fractions, as is sensible from the width of the band of $R_{\max}$, which denotes the difference of sensitivity for a given $m_{\tilde{g}}$. This difference can change by a factor of 10 when $m_{\tilde{g}} < 1000$ GeV, which can be attributed to the fact that when the cross section of $pp \to \tilde{g}\tilde{g}$ is large enough and the branching fractions of $\tilde{g} \to b\bar{b} + \not{E}_T$ and $\tilde{g} \to t\bar{t} + \not{E}_T$ are large enough, the constraint of the M_{T2} analysis method with b tagging will always perform well, though the branching fraction of $\tilde{g} \to t\bar{t}\not{E}_T$ does modify the sensitivity to some degree. When $m_{\tilde{g}} > 1000$ GeV, the dominant signals might come from either $pp \to \tilde{b}_1\tilde{b}_1$ or $pp \to \tilde{t}_1\tilde{t}_1$; then the model dependence of the bounds increases.

We also notice that when the gluino is around 300–500 GeV and dominantly goes to $g + \not{E}_T$, due to

the large cross section of $pp \to \tilde{g}\tilde{g}$ and the large mass splitting between the gluino and the LSP (say larger than 100 GeV), either the M_{T2} or α_T analysis approach can be remarkably sensitive to these points. We assume that the squarks of the first two generations are heavier than 1.5 TeV; therefore, for most points the branching fraction of $\tilde{g} \to qq' + \not{E}_T$ is typically negligible.

In the right plot of Fig. 10, among these 2400 points, the statistical information on how many models are excluded by which channels is provided. It is easy to see that both the α_T and M_{T2} analysis approaches are overwhelmingly sensitive to most of the points, while the search channels with the lepton(s) (especially the multilepton channel with the required lepton number larger than $n_\ell \geq 3$, in which case the standard model background is almost vanishing) start to play a role when neutralinos and charginos are light and their production rates are large. It is also remarkable that when the gluino is light and the decay mode $\tilde{g} \to b\bar{b}\tilde{\chi}_1^0$ is dominant (say around 300–500 GeV), the search channels with b tagging can be efficient.

In Fig. 11, we project all points in the $m_{\tilde{g}} - m_{\tilde{\chi}^0}$ plane so as to compare with the experimental bounds directly, which have also been shown in Fig. 4. There are quite a lot of points outside the experimental bounds, which are excluded mainly due to the light sbottom in the mass spectra, as shown in Fig. 7.

We notice that a few points near the region [$m_{\tilde{g}} = 1050$ GeV, $m_{\tilde{\chi}_1^0} = 100$ GeV] can survive the experimental constraints. Near this region, around 50 points are deliberately generated by the MCMC method in order to examine their common features. We find that all these surviving points have heavy stops and sbottoms ($\gtrsim$800 GeV), and then the decay channels for $\tilde{g} \to t\bar{t}$ and $\tilde{g} \to b\tilde{b}$ are below or near the kinematic threshold regions. Consequently, most of the cascade decay chains of the gluino are quite lengthy and (B) jets from direct gluino decay are relatively soft. In most cases, final states from gluino decay are soft, which weakens the bounds derived from $\tilde{g} \to t\tilde{t}$ and $\tilde{g} \to b\tilde{b}$. One interesting observation is that more than four soft leptons can show up in the final states, but the current bounds from multilepton channels cannot exclude these points.

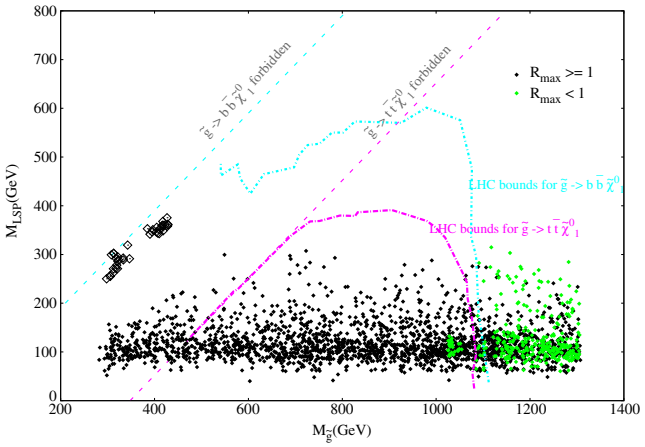

FIG. 11 (color online). The scatter points projected in the $m_{\tilde{g}} - m_{\tilde{\chi}^0}$ plane are provided, where the black points are heavily disfavored and the green points are safe. The gluino-LSP coannihilation regions of points [300,300] and [400, 360] are denoted by empty diamonds.

In order to examine the points near the gluino-LSP coannihilation region, in the first case, we deliberately introduce 200 extra points, which are denoted by an empty diamond near the points [300,300] and [400, 360] in Fig. 11. We find that these points can be excluded by both the search channel of monojet $+ \not{E}_T$ and the search channel of jets $+ \not{E}_T$.

It is remarkable that for these coannihilation points, the search channel of jets plus $\not{E}_T$ (say, B jets $+ \not{E}_T$, M_{T2} and α_T analysis approaches) has a better sensitivity than the monojet plus $\not{E}_T$ channel. The underlying reason for this is the large fraction of boost data in the signal events (about 3%–6% of the total cross section of $pp \to \tilde{g}\tilde{g}$) when compared with the cross section of the monojet events after using the monojet search cuts (about 1%–2% of the total cross section of $pp \to \tilde{g}\tilde{g}$).

For the second case, there is no coannihilation region with a mass splitting smaller than 20 GeV. We notice the bound of the gluino mass is close to the simplified model due to the large mass splitting $\Delta m = m_{\tilde{g}} - m_{\tilde{\chi}_1^0}$ and the energetic final states.

We have used the MCMC method to sample the parameter space so that we can explore the features of the natural NMSSM after taking into account the experimental constraints (except the LHC direct SUSY search bounds). In our MCMC sampling, we have simplified the Higgs experimental bounds by using the LHC data in Table I. Furthermore, we only use the code built into the NMSSMTools to examine the physics minima. To be more realistic, we have examined our 2400 points which are chosen for a collider study by using the dedicated package "vevacious" [153] (which has become available recently) to check the physics minima, so as to guarantee that the physics minimum is the global one for each point, and the package "HiggsBounds3.8.1" [154] (we have used the interface for NMSSM with HiggsBounds3.8.1 provided in [155]) to thoroughly check the experimental bounds for the Higgs boson. Around 9% (13%) of the 2400 points fail when the more dedicated package vevacious (HiggsBounds3.8.1) is adopted, while all our proposed benchmark points have passed the examination of these two dedicated packages.

IV. BENCHMARK POINTS

We examine benchmark points recommended in the literature in this section. We consider six benchmark points, labeled by "NMP" in Table III, of NMSSM listed in [157]

TABLE III. The maximal ratio of $r = N/N_{\rm exp}$ in each category of all channels is shown here, where N denotes the number of events after all cuts and $N_{\rm exp}$ denotes the allowed number of events by experiment. Superscripts and subscripts denote the LHC Collaboration (A means ATLAS and C means CMS), the collision energy ($\sqrt{s} = 7$ TeV and $\sqrt{s} = 8$ TeV) and the search channel, respectively. The label "tmp" in the fifth column denotes the results obtained by the template approach used by the CMS Collaboration [156].

	jets + $\not{E}_T$	B-jets + $\not{E}_T$	B-jets + leptons + $\not{E}_T$	leptons + jets + $\not{E}_T$	Multilepton (ML)
NMP1	$20^{C7}_{M_{T2}}$	$9.7^{C7}_{\rm BJ,\alpha_T}$	$7.7^{C8}_{\rm 2\,SSL+BJ}$	$8.1^{C7}_{\rm 1L(tmp)}$	$1.4^{C7}_{\rm ML}$
NMP2	$20^{C7}_{M_{T2}}$	$11^{C7}_{\rm BJ,\alpha_T}$	$8.3^{C8}_{\rm 2SSL+BJ}$	$6.8^{A8}_{\rm 2SSL}$	$1.4^{C7}_{\rm ML}$
NMP3	$24^{C7}_{M_{T2}}$	$12^{C7}_{\rm BJ,\alpha_T}$	$7.9^{C8}_{\rm 2SSL+BJ}$	$9.2^{C7}_{\rm 1L(tmp)}$	$1.7^{C7}_{\rm ML}$
NMP4	$23^{C7}_{M_{T2}}$	$12^{C7}_{\rm BJ,\alpha_T}$	$6.6^{C8}_{\rm 2SSL+BJ}$	$12^{C7}_{\rm 1L(tmp)}$	$2.0^{C7}_{\rm ML}$
NMP5	$22^{C7}_{M_{T2}}$	$12^{C7}_{\rm BJ,\alpha_T}$	$7.2^{C8}_{\rm 2SSL+BJ}$	$11^{C7}_{\rm 1L(tmp)}$	$1.8^{C7}_{\rm ML}$
NMP6	$6.3^{C7}_{M_{T2}}$	$2.4^{C7}_{\rm BJ,\alpha_T}$	$2.2^{A8}_{\rm 1L+BJ}$	$4.3^{C7}_{\rm 1L+Jets}$	$0.47^{C7}_{\rm ML}$
EHP1	$2.6^{C7}_{M_{T2}}$	$2.2^{C7}_{\rm BJ,\alpha_T}$	$0.4^{A8}_{\rm 1L+BJ}$	$1.3^{C7}_{\rm 2SSL+Jets}$	$0.48^{C7}_{\rm ML}$
EHP2	$2.0^{C7}_{M_{T2}}$	$1.4^{C7}_{\rm BJ,\alpha_T}$	$0.57^{A8}_{\rm 1L+BJ}$	$1.1^{C7}_{\rm 1L+Jets(tmp)}$	$0.57^{C7}_{\rm ML}$
DET1	$0.46^{C7}_{M_{T2}}$	$0.34^{C7}_{\rm BJ,\alpha_T}$	$0.04^{C8}_{\rm 2SSL+BJ}$	$0.21^{C7}_{\rm 1L(tmp)}$	$0.33^{C7}_{\rm ML}$
DET2	$0.91^{C7}_{M_{T2}}$	$0.52^{C7}_{\rm BJ,\alpha_T}$	$0.19^{C8}_{\rm 2SSL+BJ}$	$0.54^{C7}_{\rm 1L(tmp)}$	$0.39^{C7}_{\rm ML}$
$\delta M_{\tilde{\tau}}$	$1.2^{A7}_{\rm 0L+Jets}$	$3.1^{C7}_{\rm BJ,\alpha_T}$	$0.69^{C8}_{\rm 2SSL+BJ}$	$1.7^{A7}_{\rm 2L+Jets}$	$9.96^{C7}_{\rm ML}$

and find that all of them have been excluded by experiment to a quite high confidence level. We also check two benchmark points labeled as "EHP" of NMSSM from [158] and two benchmark points labeled as "DET" of NMSSM from [38]. We also examine the so-called light slepton benchmark point ($\delta M_{\tilde{\tau}}$) compiled in Table 2 of [3] with a light slepton sector inspired by the anomalous magnetic moment of the muon of the phenomenological minimal supersymmetric standard model (where both the stop and the sbottom are also light).. For each of the benchmark points, we perform the same analysis as for the points given in Sec. III. The bounds obtained from each channel are listed in Table III.

We present our results in the following form: $R^{A/C}_{\rm search\ channel\ signal\ region}$, where R is the maximum ratio of $N_{\rm sig}/N_{\rm ul}$ among all the search channels in each category of signal regions. The letter "A" stands for the ATLAS Collaboration, while the letter "C" stands for the CMS Collaboration.

For the original benchmark points labeled as NMP and proposed in [157], we observe that the search for the first two generation squarks rules out all of them. So we modify the mass of the first two generation squarks to 1.5 TeV. We notice that the first six benchmark points are very similar in spectra and decays. Each of these six benchmark points has a gluino mass around 700–800 GeV with electroweakinos lighter than ~500 GeV. We notice that for all six benchmark points, the gluino dominantly decays to $\tilde{t}_1 t$. Therefore, it is no surprise that the search channels, like B-jet(s) + $\not{E}_T$, lepton + B-jet + jets + $\not{E}_T$, and same-sign lepton + B-jet + jets + $\not{E}_T$, are sensitive to the signals of these points. Because of the large mass splitting $\Delta m = m_{\tilde{g}} - m_{\tilde{\chi}^0_1}$, the gluino-LSP coannihilation cannot occur, which consequently yields energetic visible final states when the gluino goes to the LSP and thus leads to stringent constraints for all these benchmark points.

As observed in [20], these benchmark points can survive the light stop search bounds when only part of the direct search bounds are applied. When more direct search bounds are applied, it is possible to save these six benchmark points by assuming that the gluino mass is higher than 1.5 TeV, as done in [20]. Except for the gluino mass, for the third benchmark point, the stop mass must be higher (say 500 GeV, for instance).

For the two benchmark points labeled as EHP and proposed in [158], it is observed that the most stringent bound is obtained from the search channels jets+$\not{E}_T$, B-jets + $\not{E}_T$ (with the α_T and M_{T2} analysis approaches), and lepton + jets + $\not{E}_T$, which are sensitive to the signal from the production process $pp \to \tilde{t}_1\tilde{t}_1$. These two benchmark points have been studied in [20] and have been found to be marginally safe when only the ATLAS analysis with $2B$-jets + $\not{E}_T$ by using the 2.05 fb^{-1} data set and the CMS analysis with $2B$-jets + $\not{E}_T$ by using the 4.98 fb^{-1} data set with $\sqrt{s} = 7$ TeV are applied. However, with more analysis at higher luminosity from ATLAS and CMS, these two benchmark points may fall into trouble because of the light top squark they have. They can only become safe when the top squark mass is lifted up to 600 GeV.

The two benchmark points labeled as "DET" and proposed recently in [38] are still marginally safe. The dominant signals of these two benchmark points are from the process $pp \to \tilde{t}\tilde{t}$, though the signals from the electroweakino's pair production are also considerable. It is observed that the M_{T2} analysis method can put even more stringent bounds than other analysis methods. When the updated

TABLE IV. Benchmark points for future LHC runs are tabulated.

Points	I	II	III	IV
λ	0.648	0.673	0.349	0.499
κ	0.323	0.252	0.415	0.140
$\tan\beta$	2.71	2.68	22	9.8
$\mu_{\rm eff}$	303	509	116	213
A_λ	641	1208	2626	2261
A_κ	−362	−231	−446	−110
$M_{\tilde{Q}_3}$	970	938	854	811
$M_{\tilde{U}_3}$	808	620	980	964
$M_{\tilde{D}_3}$	275	763	820	957
A_t	1792	1450	1745	1833
A_b	−60.6	−2903	2887	2910
M_1	854	530	786	522
M_2	964	269	493	260
M_3	1094	1013	1155	1174
$M_{\tilde{L}}$	380	371	212	322
m_{H_1}	**125.7**	**125.8**	118	95
m_{H_2}	191	335	**126.2**	**126.3**
m_{H_3}	827	1431	2625	2186
m_{A_1}	424	392	421	149
m_{A_2}	824	1429	2625	2186
$m_{H^\pm}$	819	1425	2625	2184
$m_{\tilde{g}}$	1209	1130	1267	1285
$m_{\tilde{\chi}_1^0}$	260	260	99	98
$m_{\tilde{\chi}_2^0}$	−324	381	−129	208
$m_{\tilde{\chi}_3^0}$	358	496	295	−235
$m_{\tilde{\chi}_4^0}$	841	−523	518	317
$m_{\tilde{\chi}_5^0}$	979	570	775	517
$m_{\tilde{\chi}_1^\pm}$	299	263	114	181
$m_{\tilde{\chi}_2^\pm}$	979	532	519	317
$m_{\tilde{t}_1}$	746	589	790	741
$m_{\tilde{t}_2}$	1064	993	1081	1063
$m_{\tilde{b}_1}$	332	795	848	834
$m_{\tilde{b}_2}$	996	958	878	991
$m_{\tilde{\nu}_L}$	376	367	202	316
$m_{\tilde{e}_L/\tilde{\mu}_L}$	382	373	217	325
$m_{\tilde{e}_R/\tilde{\mu}_R}$	381	373	216	325
$m_{\tilde{\tau}_1}$	380	370	206	319
$m_{\tilde{\tau}_2}$	383	376	227	331
$BR(B^+\to\tau^+\nu_\tau)\times 10^4$	1.32	1.32	1.31	1.32
$BR(B\to X_s\gamma)\times 10^4$	3.63	3.40	3.89	3.56
$BR(B_s\to\mu^+\mu^-)\times 10^9$	3.68	3.68	3.69	3.68
Ωh^2	0.006	0.003	0.01	0.10
$\sigma_p^{SI}(pb)\times 10^9$	26.6	31.2	3.2	1.1
$R_{\gamma\gamma}^H$	1.06	1.02	1.25	1.14
R_{VV}^H	1.03	1.0	0.98	1.05
$BR(\tilde{g}\to\tilde{t}_1 t)(\%)$	34	65	46	53
$BR(\tilde{g}\to\tilde{b}_1 b)(\%)$	59	27	28	30
$BR(\tilde{g}\to\tilde{b}_2 b)(\%)$	7	8	26	15

SUSY bounds are taken into account, only the first point is marginally safe.

For the light slepton benchmark point labeled as "$\delta M_{\tilde{\tau}}$" and compiled in [3], although the gluino is heavy, this point has been excluded by the LHC experiments. The most sensitive channel is from the multilepton search mode due to the large cross sections of sleptons and electroweakinos' pair production; other search channels sensitive to colored objects also disfavor this point due to its light stop and sbottom.

Based on our analysis, we propose four benchmark points tabulated in Table IV which are safe and can be examined for the future LHC runs.

For each case, two benchmark points are presented (the mass of the LHC Higgs is shown in boldface). For the first case, benchmark point I has a very light sbottom, ∼300 GeV, which survives from the constraints of the SUSY direct search, owing to a heavy LSP (260 GeV). Such a benchmark point might be probed by the full data set collected with $\sqrt{s}=8$ TeV, as shown in [159]. Benchmark point II has a relatively light stop (589 GeV), which dominantly decays to $\tilde{\chi}_2^0 t(29\%)$ and $\tilde{\chi}_2^+ b(61\%)$ with $\tilde{\chi}_2^0\to\tilde{\chi}_1^\pm W^\mp(90\%)$ and $\tilde{\chi}_2^\pm\to\tilde{\chi}_1^\pm Z(32\%)$, $\tilde{\chi}_1^\pm H_1(23\%)$, $\tilde{\chi}_1^0 W^\pm(26\%)$, $\tilde{\chi}_2^0 W^\pm(13\%)$. Longer cascade decay chains result in more objects in the final state, many of which are too soft to be reconstructed by detectors of the LHC.

For the second case, benchmark points III and IV have relatively heavier stops and sbottoms, which are safe from current LHC constraints. However, in point IV all five neutralinos and two charginos are very light (wino masses are only 317 GeV). It is expected that the neutralino-chargino search (mainly through trilepton and same-sign lepton signals) at the LHC should be sensitive to this point and that this point gets the correct relic density by virtue of the large singlino component(∼64%) of the LSP, while the other three points have a mostly Higgsino-like (I and III) or Wino-like (II) LSP.

We notice that masses of the gluinos are around ∼1100–1300 GeV. The main branching fractions of dominant decay modes of the gluino are tabulated. As one can see, the gluino will dominantly decay to $\tilde{t}_1 t$ and $\tilde{b}_{1/2} b$, which are exactly the representative simplified models explored by ATLAS and CMS. These benchmark points can be detected in the future LHC runs. The recent SUSY search results with $\sqrt{s}=8$ TeV presented in the Moroind 2013 EW could be sensitive to these points.

Another interesting fact is that all the sleptons are lighter than ∼500 GeV. Currently, LHC results cannot impose meaningful constraints on slepton sectors. (The LHC results can probe the sletpons with masses up to 200 GeV.) The future LHC runs at higher collision energies, either $\sqrt{s}=13$ or $\sqrt{s}=14$ TeV, can start to probe them.

V. VALIDATION OF OUR RESULTS

In order to test the reliability of the results, we perform a thorough check of our package. We have used 21 test points in total to compare with experimental results. These 21 test points have been tabulated in Table V, where TP1-7 denotes

TABLE V. All test points are tabulated.

	M_0	$M_{1/2}$			$M_{\tilde{\chi}_2^0/\tilde{\chi}_1^\pm}$	$M_{\tilde{\chi}_1^0}$			$M_{\tilde{g}}$	$M_{\tilde{\chi}_1^0}$	
TP1	210	285	CMSSM, LM1	EW1	400	200		GB1	800	300	
TP2	230	360	CMSSM, LM5	EW2	500	300	$\tilde{\chi}_2^0 \to l\tilde{l}(BF=0.5), \tilde{\chi}_1^\pm \to l\tilde{\nu}, \nu\tilde{l}$	GB2	1000	400	$\tilde{g} \to b\bar{b}\tilde{\chi}_1^0$
TP3	85	400	CMSSM, LM6	EW3	400	250		GB3	1050	550	
TP4	500	500		EW4	400	100		GT1	700	100	
TP5	700	600		EW5	350	150	$\tilde{\chi}_2^0 \to l\tilde{l}(BF=1), \tilde{\chi}_1^\pm \to \nu_\tau\tilde{\tau}_R$	GT2	800	150	
TP6	1450	175	CMSSM, LM9	EW6	200	75		GT3	900	250	$\tilde{g} \to t\bar{t}\tilde{\chi}_1^0$
TP7	2000	300		EW7	200	50	$\tilde{\chi}_2^0 \to Z\tilde{\chi}_1^0, \tilde{\chi}_1^\pm \to W^\pm\tilde{\chi}_1^0$	GT4	1000	350	

benchmark points of the CMSSM, as shown in Fig. 12. GBs and GTs are benchmark points of the simplified model, with $\tilde{g} \to t\bar{t}\tilde{\chi}_1^0$ or $\tilde{g} \to b\bar{b}\tilde{\chi}_1^0$, with a branching fraction of 100%. In addition, the test points labeled as "EW1-EW7" denote specific benchmark points designed for the electroweakinos' search [160], whose decay modes are also displayed. For test points "EW1-EW5," we assume $m_{\tilde{l}} = 0.5m_{\tilde{\chi}_1^\pm} + 0.5m_{\tilde{\chi}_1^0}$.

The results of the 21 points are tabulated in Table VI. In the table, search channels are arranged by the ATLAS and CMS collaborations and by collider energies, with data sets of $\sqrt{s} = 7$ TeV first, followed by the data sets of $\sqrt{s} = 8$ TeV. For the multilepton channel, we list the check results separately.

In each row of Table VI, one can read the results for each search channel. For example, we notice that the search channel "1-2B-jets + 1-2L" is insensitive to all our test points, since this channel is designed for a very light stop (with a mass similar to, or lighter than, the top quark) search.

From Table VI, we can observe that for test points "TP1-TP7," "GB1-GB3," and "GT1-GT4," the M_{T2} observable is quite sensitive to most of the signals, similar to our observations in Sec. III. Furthermore, the results for the "Multilepton" search channel also agree very well with experimental ones [160]. It is also obvious that the sensitivity of a specific search channel can perform better for the data set of $\sqrt{s} = 8$ TeV than that of $\sqrt{s} = 7$ TeV due to the enhancement of cross sections, as demonstrated in the channels "Multijet" of ATLAS and "2SSL + B-jets"of CMS.

In the "Jets + MHT" search channel, one can see that for seven CMSSM test points, all are excluded except for TP5 and TP7, which is in agreement with the results of CMS-7 TeV, as shown in Fig. 12. The result for GB1 shows a minor deviation. As shown in Fig. 13, this test point should have been excluded by the search channel "Jets + $\not{H}_T$," while our result underestimates the constraint with an $R_{\max} = 0.8$.

We observe that most of our results agree with experimental results, though there are some results showing deviations. For example, the "GB3" is underconstrained by the 2SSL + B-jets channel, and the "GT4" is overconstrained by the M_{T2} analysis approach and is underconstrained by the multijet channel. Compared with experimental results, these deviations of R values in Table VI can typically be

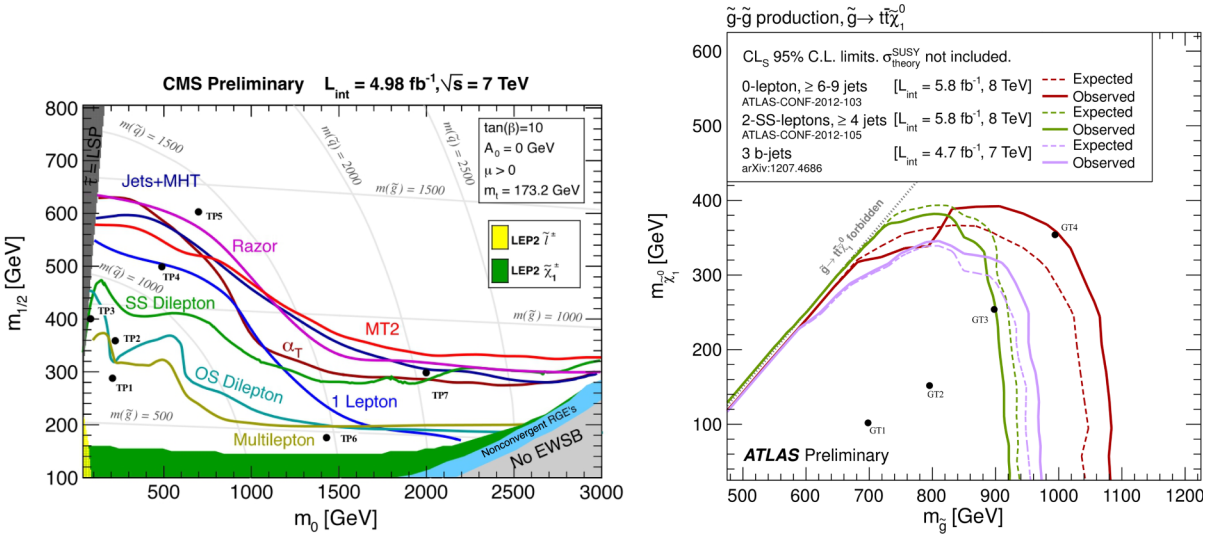

FIG. 12 (color online). Test points labeled as TP1-TP7 of the CMSSM in the $m_0 - m_{1/2}$ plane and those labeled as GT1-GT4 in the simplified models are displayed in comparison with experimental results.

TABLE VI. Results for each individual search channel are presented. Numbers in the table are defined as $R = N_{\rm sig}/N_{UL}$, where $R > 1$ means excluded by experiments. The cells with "…" mean that we have not looked at these channels since the signal is expected to vanish.

	TP1	TP2	TP3	TP4	TP5	TP6	TP7	GB1	GB2	GB3	GT1	GT2	GT3	GT4
Jets	21	12	7.6	6.4	1.6	5.4	1.4	1.3	0.42	0.16	2.9	1.9	0.84	0.37
Multijet	1.7	0.72	0.13	0.11	0.02	2.3	0.63	0.09	0.02	0.01	1.8	0.79	0.29	0.11
B jets	4.1	2.2	0.39	0.24	0.04	3.6	0.56	4.8	0.86	0.45	4.8	2.2	0.91	0.37
Jets [heavy stop]	17	6.1	1.8	0.59	0.09	7.4	1.1	1.8	0.33	0.18	5.9	3.2	1.4	0.63
1-2B-jets + 1-2L	0	0	0	0	0	0	0	0	0	0	0	0	0	0
2L + jets	0.07	0.01	0.05	0	0	0.15	0.01	0	0	0	0.01	0	0	0
2L + jets [medium stop]	1	0.36	0.54	0.06	0.01	0.28	0.09	0	0	0	0.76	0.33	0.12	0.06
1L + jets	3.6	0.95	0.73	0.10	0.02	1.0	0.24	0	0	0	2.8	1.2	0.47	0.19
Multijet	18	7.8	5.0	1.5	0.17	1.8	0.27	0.80	0.27	0.11	0.46	0.39	0.19	0.09
M_{T2}	50	26	9.5	3.9	0.68	42	5.9	8.4	1.6	0.81	16	6.4	2.5	1.0
B jets	9	5.6	2.6	0.91	0.17	2.9	0.37	3.2	0.53	0.30	2.6	1.4	0.59	0.24
(B) jets, α_T	57	25	13	3.8	0.63	30	3.1	2.5	0.71	0.25	4.7	2.2	0.84	0.31
1L + B jets	1.0	0.66	0.31	0.08	0.01	0.58	0.37	0	0	0	2.6	1.2	0.45	0.18
2SSL + B jets	2.4	0.64	0.94	0.07	0.01	1.4	0.59	0	0	0	4.4	1.9	0.67	0.26
1L (tmp)	7.1	4.6	2.9	0.74	0.14	2.3	1.4	0	0	0	5.7	3.4	1.5	0.63
2SSL	11	5.4	4.5	0.39	0.06	15	1.4	0.09	0.01	0.01	7.2	2.7	1.0	0.38
2OSL	11	5.3	4.3	0.58	0.09	3.7	0.78	0.05	0.01	0.01	2.7	1.3	0.57	0.25
τ(s) + jets	24	11	6.3	1.0	0.16	4.4	0.45	0.54	0.15	0.07	1.4	0.65	0.26	0.13
Z boson + jets	5.9	0.35	0.94	0.05	0.01	0.37	0.15	0	0	0	0.27	0.11	0.04	0.02
Monojet	4.2	1.4	1.2	0.12	0.02	0.03	0.01	0.02	0	0	0	0	0	0
	EW1	EW2	EW3	EW4	EW5	EW6	EW7	…	…	…	…	…	…	…
Multilepton	2.0	0.61	0.81	1.5	1.2	0.61	0.77	…	…	…	…	…	…	…
Multijet	…	…	…	…	…	…	…	…	…	…	2.8	2.2	1.2	0.60
Jets	…	…	…	…	…	…	…	…	…	…	4.2	1.8	0.79	0.32
2SSL	…	…	…	…	…	…	…	…	…	…	4.4	2.7	1.3	0.61
1L + jets	…	…	…	…	…	…	…	…	…	…	5.5	2.1	0.88	0.35
2SSL + B jets	…	…	…	…	…	…	…	…	…	…	4.9	2.4	1.1	0.42

around ±30% or so, which can only affect the results of those points near the exclusion edges of experimental results. For example, the results of GB3 and GT4 should be excluded by the corresponding experimental search channels, but can survive in our analysis. When a point is far away from the edge and inside the exclusion region, our results are trustable, like the test point "GT1."

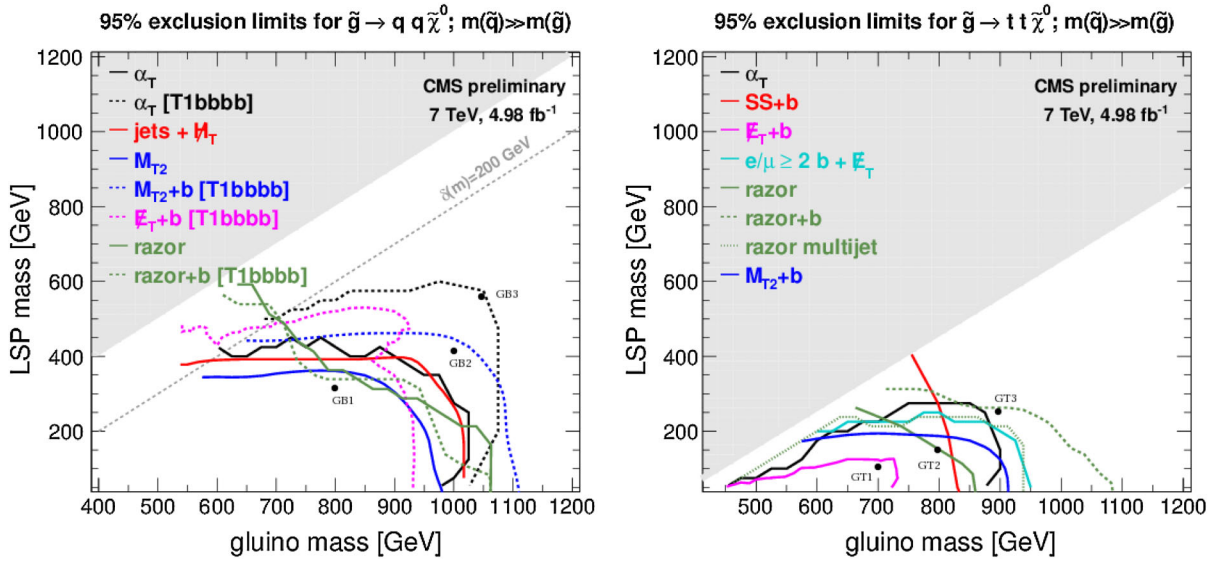

FIG. 13 (color online). Test points labeled as GB1-GB3 and GT1-GT3 in the simplified models are displayed in comparison with experimental results.

Meanwhile, we notice that when the gluino mass is shifted by ± 40 GeV, the deviations can be removed and agreements can be achieved. The deviations in R can be attributed to the small fluctuations from Monte Carlo simulations and the difference between the fast detector simulation and the real detector effects. Our bottom line is that our results at least motivate experimentalists to perform more detailed and serious analysis when all types of uncertainties are taken into account.

VI. DISCUSSIONS AND CONCLUSIONS

We have extended the analysis [20,152] by including more LHC experimental bounds. Limited by our computing resources, we have chosen around 2400 typical points to conduct the detailed Monte Carlo study so as to study the constraints from the direct LHC searches on the gluino mass. We have checked that the distributions of the chosen 2400 points are similar to those of 10 million points; therefore, results for these 2400 points are representative of the 10 million points. Obviously, our method cannot guarantee that all of the interesting regions in parameter space have been sufficiently sampled, like some specific theoretical models defined on some hyperbolic surfaces in the parameter space and situated in the parameter space as isolated islands. We hope this study inspires experimentalists to conduct a more thorough and strict study on the natural NMSSM. We believe that, from these 2400 points, we can extract the useful information on how the experiments may constrain the models, especially on the light gluino scenarios in the context of the natural NMSSM where the gluino dominantly decays to $t\tilde{t}$, $b\tilde{b}$, and $g\tilde{\chi}_1^0$.

The central question of this study is how the experimental bounds on the gluino mass from $\tilde{g} \to g\tilde{\chi}_1^0$, $\tilde{g} \to t\tilde{t}$, and $\tilde{g} \to b\tilde{b}$ should constrain the natural NMSSM defined in Eq. (5). In the simplified models used by experimentalists, only a few parameters play roles in the final states: say $m_{\tilde{g}}$, $m_{\tilde{\chi}_1^0}$, $m_{\tilde{t}}$, and $m_{\tilde{b}}$.

In the natural NMSSM, more model parameters can affect the signal via changing branching fractions, as demonstrated in Figs. 8–10. Although there is greater than 16-dimensional space in the natural NMSSM, in most cases, the key and active parameter space determining the gluino bounds includes $m_{\tilde{g}}$, $m_{\tilde{\chi}_1^0}$, $m_{\tilde{\chi}_1^\pm}$, $m_{\tilde{t}}$, $m_{\tilde{b}}$, and $m_{\tilde{\ell}}$ as well as some couplings that determine branching fractions, of which the number is less than 15. Our study with 2400 points reveals that the gluino mass is the dominant factor determining whether a model is ruled out or not. Meanwhile, the decay chains could also play an important role. For example, for a given gluino mass (say $m_{\tilde{g}} = 700$ GeV), the model dependence can change the $R_{\max}$ by a factor of 20–30 or so, as can be seen from the plots in the lower row of Fig. 8.

Based on our understanding of our approach and on the analysis shown above, we comment on light gluino models in the literature. Models in the coannihilation region as demonstrated by LG3-5, given in [58], can be ruled out due to the monojet search and by the α_T and M_{T2} analyses (due to the boosted sample events) from the CMS if the branching fraction $\tilde{g} \to g\tilde{\chi}_1^0$ is dominant. Because of the large mass splitting between the gluino and the LSP and the energetic final states, light gluino scenarios with a mass range [500,700] GeV in the so-called Higgs pole region of the minimal universal SUGRA [161] are heavily disfavored. The two benchmark points presented in Ref. [61] have been excluded due to their large cross sections and large mass splittings. We also find that even for the coannihilation region (say $m_{\tilde{g}} - m_{\tilde{\chi}^0} < 20$ GeV), the monojet bounds can be valid for a gluino mass up to 400 GeV at least, as shown by the right plot of Fig. 9.

It might be beneficial to comment on the difference of the MSSM, and here we focus on collider physics. In the NMSSM, the existence of an extra light singlet superfield can have a great influence on the sparticle decay. Because the singlet does not couple to SM particles, the produced sparticles are more likely to decay into heavier charginos and neutralinos, which finally go to the singlet-like LSP via cascade decay chains; i.e. the longer decay chain can lead to multijets or extra leptons in the final state. Furthermore, the existence of the singlino LSP makes those scenarios available where the LSP might be charged and colored in the MSSM. More interestingly, the Higgs mass can get an additional tree-level contribution in the NMSSM. Thus, the parameter space with a relatively light stop and small mixing in the stop sector can be consistent with experimental data, which is especially important for scenario II in this work, where the LSP is singlino dominant and light. The singlino dominant LSP can also affect the dark matter search significantly, as carefully explored in [152].

Last but not least, since we confine ourselves to the natural NMSSM defined in Eq. (5), there is no point near the region $m_{\tilde{g}} \approx m_{\tilde{\chi}^0} \sim 500$ GeV that is allowed. However, such models with heavier $m_{\tilde{\chi}^0}$ could exist, as demonstrated in Fig. 8c of [162] by red points, where the scanning ranges for parameters of the neutralino and gluino are wider than those in our scanning.

With the results shown above, we would like to conclude on the natural NMSSM defined in Eq. (5): (1) Its parameter space has been significantly shrunken by the direct SUSY search bounds from the ATLAS and CMS collaborations. (2) The gluino-LSP coannihilation region in the first case of interpretations of the Higgs boson data can hardly pass the experimental constraints due to the boosted signal samples. The gluino mass can be ruled out up to 400 GeV for the gluino-LSP coannihilation region. (3) For the region where the mass splitting of the gluino and LSP is large enough (say > 600 GeV) and the gluino dominantly goes to $t\bar{t}\tilde{\chi}_1^0$ and $b\bar{b}\tilde{\chi}_1^0$, we find that experiments can rule out points

with a gluino mass larger than 1 TeV or so, as shown in Fig. 11.

ACKNOWLEDGMENTS

We would like to thank Chunli Tong for his contribution to the MCMC method at the early stage of this project. We also thank Qiang Yuan and Hong Li from IHEP, CAS for their explanations of the MCMC method. We are indebted to Zhen-Wei Yang and Yuan-Ning Gao from the HEP group of Tsinghua University and Xiao-Rui Lv and Yang-Heng Zheng from UCAS for help using the PC farms of their groups. This research was supported in part by the Natural Science Foundation of China under Grants No. 10821504, No. 11075194, No. 11135003, No. 11275246 (T. C., J. L., T. L.), and No. 11175251 (Q. Y.), and by the DOE Grant No. DE-FG03-95-Er-40917 (T. L.).

Note added.—When this work was finished, in the updated results presented at the Rencontres de Moroind 2013 EW, we noticed that points with a gluino mass heavier than 1.2 TeV can be ruled out when the squarks of the third generation are assumed to be light. Experimental bounds nearly approach the upper limit of the gluino mass of the natural SUSY models.

[1] G. Aad *et al.* (ATLAS Collaboration), Phys. Lett. B **716**, 1 (2012).
[2] S. Chatrchyan *et al.* (CMS Collaboration), Phys. Lett. B **716**, 30 (2012).
[3] H. Baer and J. List, arXiv:1205.6929.
[4] J. L. Feng, Annu. Rev. Nucl. Part. Sci. **63**, 351 (2013).
[5] M. Papucci, J. T. Ruderman, and A. Weiler, J. High Energy Phys. 09 (**2012**) 035.
[6] G. Anderson, C. H. Chen, J. F. Gunion, J. D. Lykken, T. Moroi, and Y. Yamada, eConf C960625 (1996).
[7] S. P. Martin, Phys. Rev. D **75**, 115005 (2007).
[8] P. Draper, P. Meade, M. Reece, and D. Shih, Phys. Rev. D **85**, 095007 (2012).
[9] Z. Kang, T. Li, T. Liu, C. Tong, and J. M. Yang, Phys. Rev. D **86**, 095020 (2012).
[10] N. Craig, S. Knapen, D. Shih, and Y. Zhao, J. High Energy Phys. 03 (**2013**) 154.
[11] B. de Carlos and J. A. Casas, Phys. Lett. B **309**, 320 (1993); P. H. Chankowski, J. R. Ellis, and S. Pokorski, Phys. Lett. B **423**, 327 (1998); R. Barbieri and A. Strumia, Phys. Lett. B **433**, 63 (1998); G. L. Kane and S. F. King, Phys. Lett. B **451**, 113 (1999); L. Giusti, A. Romanino, and A. Strumia, Nucl. Phys. **B550**, 3 (1999); Z. Chacko, Y. Nomura, and D. Tucker-Smith, Nucl. Phys. **B725**, 207 (2005); R. Kitano and Y. Nomura, Phys. Lett. B **631**, 58 (2005); P. Athron and D. J. Miller, Phys. Rev. D **76**, 075010 (2007); S. Cassel, D. M. Ghilencea, and G. G. Ross, Nucl. Phys. **B825**, 203 (2010); R. Barbieri and D. Pappadopulo, J. High Energy Phys. 10 (**2009**) 061; M. Asano, H. D. Kim, R. Kitano, and Y. Shimizu, J. High Energy Phys. 12 (**2010**) 019.
[12] S. Antusch, L. Calibbi, V. Maurer, M. Monaco, and M. Spinrath, J. High Energy Phys. 01 (**2013**) 187; I. Gogoladze, F. Nasir, and Q. Shafi, Int. J. Mod. Phys. A **28**, 1350046 (2013); H. Baer, V. Barger, P. Huang, D. Mickelson, A. Mustafayev, and X. Tata, Phys. Rev. D **87**, 115028 (2013).
[13] Z. Kang, J. Li, and T. Li, J. High Energy Phys. 11 (**2012**) 024.
[14] J.-J. Cao, Z.-X. Heng, J. M. Yang, Y.-M. Zhang, and J.-Y. Zhu, J. High Energy Phys. 03 (**2012**) 086.
[15] T. Cheng, J. Li, T. Li, X. Wan, Y. k. Wang, and S.-h. Zhu, arXiv:1207.6392.
[16] K. Agashe, Y. Cui, and R. Franceschini, J. High Energy Phys. 02 (**2013**) 031.
[17] Early works: S. Chang, P. J. Fox, and N. Weiner, J. High Energy Phys. 08 (**2006**) 068; R. Dermisek and J. F. Gunion, Phys. Rev. D **77**, 015013 (2008).
[18] G. G. Ross and K. Schmidt-Hoberg, Nucl. Phys. **B862**, 710 (2012); G. G. Ross, K. Schmidt-Hoberg, and F. Staub, J. High Energy Phys. 08 (**2012**) 074; A. Kaminska, G. G. Ross, and K. Schmidt-Hoberg, J. High Energy Phys. 11 (**2013**) 209.
[19] U. Ellwanger, C. Hugonie, and A. M. Teixeira, Phys. Rep. **496**, 1 (2010).
[20] X.-J. Bi, Q.-S. Yan, and P.-F. Yin, Phys. Rev. D **87**, 035007 (2013).
[21] L. Aparicio, P. G. Camara, D. G. Cerdeno, L. E. Ibanez, and I. Valenzuela, J. High Energy Phys. 02 (**2013**) 084.
[22] J. R. Ellis, K. Enqvist, D. V. Nanopoulos, K. A. Olive, M. Quiros, and F. Zwirner, Phys. Lett. B **176**, 403 (1986); B. Ray and G. Senjanovic, Phys. Rev. D **49**, 2729 (1994).
[23] D. Suematsu and Y. Yamagishi, Int. J. Mod. Phys. A **10**, 4521 (1995).
[24] H.-C. Cheng, B. A. Dobrescu, and K. T. Matchev, Phys. Lett. B **439**, 301 (1998); , Nucl. Phys. **B543**, 47 (1999); D. A. Demir, Phys. Rev. D **59**, 015002 (1998).
[25] M. Cvetic and P. Langacker, Phys. Rev. D **54**, 3570 (1996); P. Langacker and J. Wang, Phys. Rev. D **58**, 115010 (1998).
[26] M. Cvetic, D. A. Demir, J. R. Espinosa, L. L. Everett, and P. Langacker, Phys. Rev. D **56**, 2861 (1997); , Phys. Rev. D **58**, 119905(E) (1998).
[27] J. F. Gunion, Y. Jiang, and S. Kraml, Phys. Rev. D **86**, 071702 (2012); Phys. Rev. Lett. **110**, 051801 (2013).
[28] G. Belanger, U. Ellwanger, J. F. Gunion, Y. Jiang, S. Kraml, and J. H. Schwarz, J. High Energy Phys. 01 (**2013**) 069.

[29] G. Belanger, U. Ellwanger, J. F. Gunion, Y. Jiang, and S. Kraml, arXiv:1208.4952.
[30] Z. Kang, J. Li, T. Li, D. Liu, and J. Shu, Phys. Rev. D **88**, 015006 (2013).
[31] N. D. Christensen, T. Han, Z. Liu, and S. Su, J. High E nergy Phys. 08 (**2013**) 019.
[32] https://twiki.cern.ch/twiki/bin/view/CMSPublic/Physics ResultsSUS.
[33] https://twiki.cern.ch/twiki/bin/view/AtlasPublic/Super symmetryPublicResults.
[34] P. Bechtle, T. Bringmann, K. Desch, H. Dreiner, M. Hamer, C. Hensel, M. Kramer, and N. Nguyen *et al.*, J. High Energy Phys. 06 (**2012**) 098.
[35] A. Fowlie, M. Kazana, K. Kowalska, S. Munir, L. Roszkowski, E. M. Sessolo, S. Trojanowski, and Y.-L. S. Tsai, Phys. Rev. D **86**, 075010 (2012).
[36] C. Beskidt, W. de Boer, D. I. Kazakov, and F. Ratnikov, Eur. Phys. J. C **72**, 2166 (2012).
[37] F. Mahmoudi, A. Arbey, M. Battaglia, and A. Djouadi, Proc. Sci., ICHEP2012 (**2013**) 124.
[38] D. Das, U. Ellwanger, and A. M. Teixeira, J. High Energy Phys. 04 (**2013**) 117.
[39] J. Cao, C. Han, L. Wu, J. M. Yang, and Y. Zhang, J. High Energy Phys. 11 (**2012**) 039.
[40] B. Bhattacherjee and K. Ghosh, arXiv:1207.6289.
[41] H. K. Dreiner, M. Kramer, and J. Tattersall, Europhys. Lett. **99**, 61001 (2012).
[42] M. Cvetic, T. Li, and T. Liu, Nucl. Phys. **B698**, 163 (2004).
[43] C.-M. Chen, T. Li, V. E. Mayes, and D. V. Nanopoulos, Phys. Lett. B **665**, 267 (2008).
[44] C.-M. Chen, T. Li, V. E. Mayes, and D. V. Nanopoulos, Phys. Rev. D **77**, 125023 (2008).
[45] T. Li, J. A. Maxin, and D. V. Nanopoulos, Phys. Lett. B **701**, 321 (2011).
[46] T. Li and D. V. Nanopoulos, Phys. Lett. B **692**, 121 (2010).
[47] B. S. Acharya, K. Bobkov, G. L. Kane, J. Shao, and P. Kumar, Phys. Rev. D **78**, 065038 (2008).
[48] N. Arkani-Hamed, A. Gupta, D. E. Kaplan, N. Weiner, and T. Zorawski, arXiv:1212.6971.
[49] N. Arkani-Hamed and S. Dimopoulos, J. High Energy Phys. 06 (**2005**) 073.
[50] G. F. Giudice, M. A. Luty, H. Murayama, and R. Rattazzi, J. High Energy Phys. 12 (**1998**) 027.
[51] J. D. Wells, arXiv:hep-ph/0306127.
[52] M. Dine, P. J. Fox, E. Gorbatov, Y. Shadmi, Y. Shirman, and S. D. Thomas, Phys. Rev. D **70**, 045023 (2004).
[53] G. F. Giudice and A. Romanino, Nucl. Phys. **B699**, 65 (2004); , Nucl. Phys. **B706**, 65(E) (2005).
[54] G. F. Giudice and A. Strumia, Nucl. Phys. **B858**, 63 (2012).
[55] J. D. Wells, Phys. Rev. D **71**, 015013 (2005).
[56] H. Baer, V. Barger, and P. Huang, J. High Energy Phys. 11 (**2011**) 031.
[57] J. L. Hewett, B. Lillie, M. Masip, and T. G. Rizzo, J. High Energy Phys. 09 (**2004**) 070.
[58] N. Chen, D. Feldman, Z. Liu, P. Nath, and G. Peim, Phys. Rev. D **83**, 035005 (2011).
[59] G. F. Giudice, T. Han, K. Wang, and L.-T. Wang, Phys. Rev. D **81**, 115011 (2010).
[60] B. S. Acharya, P. Grajek, G. L. Kane, E. Kuflik, K. Suruliz, and L.-T. Wang, arXiv:0901.3367; G. L. Kane, E. Kuflik, R. Lu, and L.-T. Wang, Phys. Rev. D **84**, 095004 (2011).
[61] M. Adeel Ajaib, T. Li, Q. Shafi, and K. Wang, J. High Energy Phys. 01 (**2011**) 028.
[62] D. Feldman, Z. Liu, and P. Nath, Phys. Rev. Lett. **99**, 251802 (2007); , Phys. Lett. B **662**, 190 (2008); J. High Energy Phys. 04 (**2008**) 054.
[63] G. Kane, R. Lu, and B. Zheng, arXiv:1202.4448.
[64] W. R. Gilks, S. Richardson, and D. J. Spiegelhalter, *661 Markov Chain Monte Carlo in Practice* (Chapman & Hall, London, 1996).
[65] R. Trotta, Contemp. Phys. **49**, 71 (2008).
[66] E. A. Baltz and P. Gondolo, J. High Energy Phys. 10 (**2004**) 052.
[67] B. C. Allanach and C. G. Lester, Phys. Rev. D **73**, 015013 (2006).
[68] B. C. Allanach, Phys. Lett. B **635**, 123 (2006).
[69] R. R. de Austri, R. Trotta, and L. Roszkowski, J. High Energy Phys. 05 (**2006**) 002.
[70] T. Burgess, J. O. Lindroos, A. Lipniacka, and H. Sandaker, J. High Energy Phys. 08 (**2013**) 098.
[71] R. Aaij *et al.* (LHCb Collaboration), Phys. Rev. Lett. **110**, 021801 (2013).
[72] D. Asner *et al.* (Heavy Flavor Averaging Group Collaboration), arXiv:1010.1589.
[73] E. Barberio *et al.* (Heavy Flavor Averaging Group (HFAG) Collaboration), arXiv:hep-ex/0603003.
[74] R. Aaij *et al.* (LHCb Collaboration), Phys. Rev. Lett. **108**, 231801 (2012).
[75] D. Larson, J. Dunkley, G. Hinshaw, E. Komatsu, M. R. Nolta, C. L. Bennett, B. Gold, and M. Halpern *et al.*, Astrophys. J. Suppl. Ser. **192**, 16 (2011).
[76] L. Baudis (XENON Collaboration), arXiv:1203.1589.
[77] S. Chatrchyan *et al.* (CMS Collaboration), Phys. Lett. B **716**, 30 (2012).
[78] G. Aad *et al.* (ATLAS Collaboration), Phys. Lett. B **716**, 1 (2012).
[79] B. C. Allanach, S. Kraml, and W. Porod, J. High Energy Phys. 03 (**2003**) 016; G. Belanger, S. Kraml, and A. Pukhov, Phys. Rev. D **72**, 015003 (2005).
[80] S. F. Daniel, A. J. Connolly, and J. Schneider, arXiv:1205.2708.
[81] Rajeeva L. Karandikar, Sadhana **31**, 81 (2006).
[82] U. Ellwanger, J. F. Gunion, and C. Hugonie, J. High Energy Phys. 02 (**2005**) 066.
[83] U. Ellwanger and C. Hugonie, Comput. Phys. Commun. **175**, 290 (2006).
[84] https://twiki.cern.ch/twiki/bin/view/AtlasPublic/ CombinedSummaryPlots#SusySummary; https://twiki.cern .ch/twiki/bin/view/CMSPublic/SUSYSMSSummaryPlots7 TeV.
[85] G. Aad *et al.* (ATLAS Collaboration), Phys. Rev. D **87**, 012008 (2013).
[86] G. Aad *et al.* (ATLAS Collaboration), Phys. Lett. B **710**, 67 (2012).
[87] ATLAS Collaboration, Report No. ATLAS-CONF-2011-155.
[88] ATLAS Collaboration, Report No. ATLAS-CONF-2011-086.

[89] G. Aad *et al.* (ATLAS Collaboration), Phys. Lett. B **701**, 186 (2011).
[90] ATLAS Collaboration, Report No. ATLAS-CONF-2010-065.
[91] G. Aad *et al.* (ATLAS Collaboration), J. High Energy Phys. 07 (**2012**) 167.
[92] G. Aad *et al.* (ATLAS Collaboration), J. High Energy Phys. 11 (**2011**) 099.
[93] G. Aad *et al.* (ATLAS Collaboration), Phys. Rev. Lett. **109**, 211802 (2012).
[94] G. Aad *et al.* (ATLAS Collaboration), Eur. Phys. J. C **72**, 2174 (2012).
[95] G. Aad *et al.* (ATLAS Collaboration), Phys. Rev. Lett. **108**, 181802 (2012).
[96] ATLAS Collaboration, Report No. ATLAS-CONF-2012-106.
[97] ATLAS Collaboration, Report No. ATLAS-CONF-2011-098.
[98] ATLAS Collaboration, Report No. ATLAS-CONF-2010-079.
[99] G. Aad *et al.* (ATLAS Collaboration), Phys. Lett. B **720**, 13 (2013).
[100] G. Aad *et al.* (ATLAS Collaboration), Phys. Rev. Lett. **109**, 211803 (2012).
[101] G. Aad *et al.* (ATLAS Collaboration), Phys. Rev. D **85**, 112006 (2012).
[102] ATLAS Collaboration, Report No. ATLAS-CONF-2011-130.
[103] G. Aad *et al.* (ATLAS Collaboration), Phys. Lett. B **701**, 398 (2011).
[104] G. Aad *et al.* (ATLAS Collaboration), J. High Energy Phys. 11 (**2012**) 094.
[105] G. Aad *et al.* (ATLAS Collaboration), Phys. Rev. D **86**, 092002 (2012).
[106] G. Aad *et al.* (ATLAS Collaboration), Eur. Phys. J. C **72**, 2237 (2012).
[107] G. Aad *et al.* (ATLAS Collaboration), Phys. Rev. Lett. **108**, 241802 (2012).
[108] G. Aad *et al.* (ATLAS Collaboration), Phys. Lett. B **709**, 137 (2012).
[109] G. Aad *et al.* (ATLAS Collaboration), Phys. Rev. D **85**, 012006 (2012).
[110] ATLAS Collaboration, Report No. ATLAS-CONF-2012-140.
[111] ATLAS Collaboration, Report No. ATLAS-CONF-2011-090.
[112] G. Aad *et al.* (ATLAS Collaboration), Eur. Phys. J. C **71**, 1682 (2011).
[113] G. Aad *et al.* (ATLAS Collaboration), Eur. Phys. J. C **71**, 1647 (2011).
[114] G. Aad *et al.* (ATLAS Collaboration), Phys. Rev. Lett. **106**, 131802 (2011).
[115] ATLAS Collaboration, Report No. ATLAS-CONF-2011-091.
[116] ATLAS Collaboration, Report No. ATLAS-CONF-2011-064.
[117] ATLAS Collaboration, Eur. Phys. J. C **72**, 2237 (2012).
[118] G. Aad *et al.* (ATLAS Collaboration), Phys. Lett. B **718**, 841 (2013).
[119] G. Aad *et al.* (ATLAS Collaboration), Phys. Lett. B **718**, 879 (2013).
[120] G. Aad *et al.* (ATLAS Collaboration), Phys. Rev. Lett. **108**, 261804 (2012).
[121] ATLAS Collaboration, Report No. ATLAS-CONF-2012-108.
[122] ATLAS Collaboration, Report No. ATLAS-CONF-2012-035.
[123] ATLAS Collaboration, Report No. ATLAS-CONF-2012-001.
[124] ATLAS Collaboration, Report No. ATLAS-CONF-2011-039.
[125] ATLAS Collaboration, Report No. ATLAS-CONF-2012-084.
[126] ATLAS Collaboration, Report No. ATLAS-CONF-2012-109.
[127] ATLAS Collaboration, Report No. ATLAS-CONF-2012-103.
[128] ATLAS Collaboration, Report No. ATLAS-CONF-2012-104.
[129] ATLAS Collaboration, Report No. ATLAS-CONF-2012-105.
[130] CMS Collaboration, Report No. CMS-PAS-SUS-12-005; S. Chatrchyan *et al.* (CMS Collaboration), J. High Energy Phys. 10 (**2012**) 018.
[131] S. Chatrchyan *et al.* (CMS Collaboration), Phys. Rev. Lett. **109**, 171803 (2012); CMS Collaboration, Report No. CMS-PAS-SUS-12-009.
[132] S. Chatrchyan *et al.* (CMS Collaboration), Phys. Rev. D **86**, 072010 (2012); CMS Collaboration, Report No. CMS-PAS-SUS-11-022; CMS Collaboration, Report No. CMS-PAS-SUS-11-024.
[133] CMS Collaboration, Report No. CMS-PAS-SUS-11-028.
[134] CMS Collaboration, Report No. CMS-PAS-SUS-12-010; CMS Collaboration, Report No. CMS-PAS-SUS-11-027; S. Chatrchyan *et al.* (CMS Collaboration), Phys. Rev. Lett. **109**, 071803 (2012); S. Chatrchyan *et al.* (CMS Collaboration), Phys. Lett. B **718**, 815 (2013);CMS Collaboration, Report No. CMS-PAS-SUS-12-004.
[135] S. Chatrchyan *et al.* (CMS Collaboration), J. High Energy Phys. 06 (**2012**) 169; S. Chatrchyan *et al.* (CMS Collaboration), arXiv:1209.6620.
[136] S. Chatrchyan *et al.* (CMS Collaboration), Phys. Lett. B **716**, 260 (2012).
[137] S. Chatrchyan *et al.* (CMS Collaboration), J. High Energy Phys. 09 (**2012**) 094.
[138] CMS Collaboration, Report No. CMS-PAS-SUS-12-004.
[139] CMS Collaboration, Report No. CMS-PAS-SUS-12-004.
[140] L. Randall and D. Tucker-Smith, Phys. Rev. Lett. **101**, 221803 (2008).
[141] S. Chatrchyan *et al.* (CMS Collaboration), J. High Energy Phys. 01 (**2013**) 077.
[142] C. G. Lester and D. J. Summers, Phys. Lett. B **463**, 99 (1999).
[143] C. Rogan, arXiv:1006.2727.
[144] A. L. Read, J. Phys. G **28**, 2693 (2002).
[145] G. Cowan, K. Cranmer, E. Gross, and O. Vitells, Eur. Phys. J. C **71**, 1 (2011).
[146] W. Beenakker, R. Hopker, and M. Spira, arXiv:hep-ph/9611232.
[147] J. Alwall, P. Demin, S. de Visscher, R. Frederix, M. Herquet, F. Maltoni, T. Plehn, D. L. Rainwater, and

T. Stelzer, J. High Energy Phys. 09 (**2007**) 028; J. Alwall, M. Herquet, F. Maltoni, O. Mattelaer, and T. Stelzer, J. High Energy Phys. 06 (**2011**) 128.

[148] T. Sjostrand, S. Mrenna, and P. Z. Skands, J. High Energy Phys. 05 (**2006**) 026.

[149] http://www.physics.ucdavis.edu/conway/research/software/pgs/pgs4-general.htm.

[150] W. Beenakker, S. Brensing, M. Kramer, A. Kulesza, E. Laenen, and I. Niessen, J. High Energy Phys. 08 (**2010**) 098.

[151] W. Beenakker, M. Kramer, T. Plehn, M. Spira, and P. M. Zerwas, Nucl. Phys. **B515**, 3 (1998).

[152] X.-J. Bi, Q.-S. Yan, and P.-F. Yin, Phys. Rev. D **85**, 035005 (2012).

[153] J. E. Camargo-Molina, B. O'Leary, W. Porod, and F. Staub, Eur. Phys. J. C **73**, 2588 (2013).

[154] P. Bechtle, O. Brein, S. Heinemeyer, G. Weiglein, and K. E. Williams, Comput. Phys. Commun. **181**, 138 (2010); Comput. Phys. Commun. **182**, 2605 (2011).

[155] D. A. Vasquez, G. Belanger, C. Boehm, J. Da Silva, P. Richardson, and C. Wymant, Phys. Rev. D **86**, 035023 (2012).

[156] S. Chatrchyan *et al.* (CMS Collaboration), Phys. Rev. D **87**, 052006 (2013); S. Chatrchyan *et al.* (CMS Collaboration), Report No. CMS-PAS-SUS-11-027.

[157] S. F. King, M. Muhlleitner, and R. Nevzorov, Nucl. Phys. **B860**, 207 (2012).

[158] U. Ellwanger and C. Hugonie, Adv. High Energy Phys. **2012**, 1 (2012).

[159] Z.-H. Yu, X.-J. Bi, Q.-S. Yan, and P.-F. Yin, Phys. Rev. D **87**, 055007 (2013).

[160] S. Chatrchyan *et al.* (CMS Collaboration), J. High Energy Phys. 11 (**2012**) 147.

[161] D. Feldman, K. Freese, P. Nath, B. D. Nelson, and G. Peim, Phys. Rev. D **84**, 015007 (2011).

[162] T. Gherghetta, B. von Harling, A. D. Medina, and M. A. Schmidt, J. High Energy Phys. 02 (**2013**) 032.